Report

Current Biology

A Transient Rise in Free Mg^{2+} Ions Released from ATP-Mg Hydrolysis Contributes to Mitotic Chromosome Condensation

Graphical Abstract

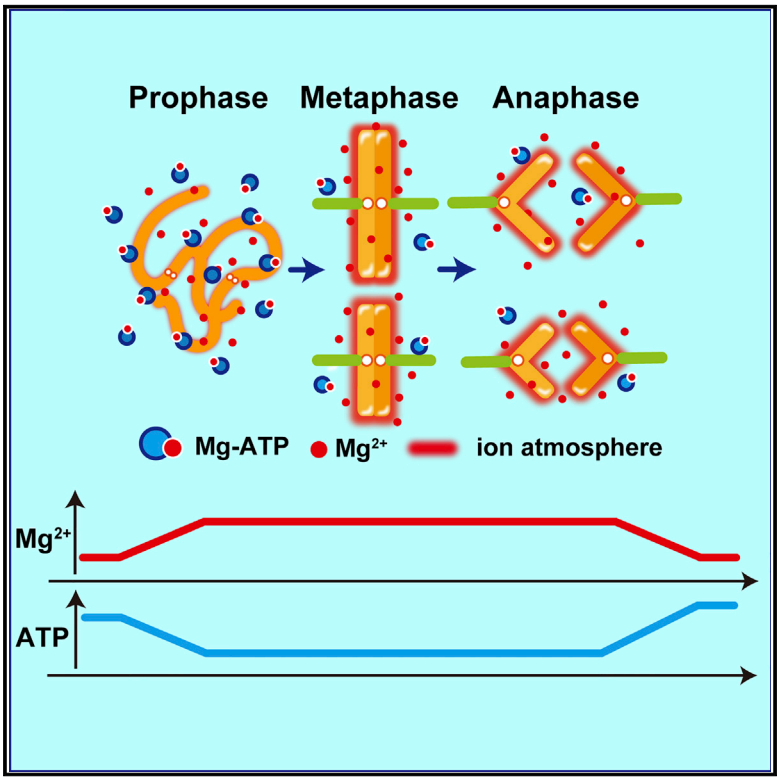

Highlights

- We developed a FRET-based Mg^{2+} indicator for live cell-cycle analysis
- During mitosis, levels of free Mg^{2+} increase and are coupled with a decrease in ATP
- ATP reduction induced chromosome hypercondensation
- Chelating Mg^{2+} had a chromosome decondensation effect

Authors

Kazuhiro Maeshima, Tomoki Matsuda, Yutaka Shindo, ..., Hiroyuki Noji, Kotaro Oka, Takeharu Nagai

Correspondence

kmaeshim@nig.ac.jp (K.M.), ng1@sanken.osaka-u.ac.jp (T.N.)

In Brief

How the negatively charged long genomic DNA is organized into mitotic chromosome remains unclear. Using a newly developed Mg^{2+} indicator, Maeshima et al. demonstrate a transient rise in free Mg^{2+} released from ATP-Mg during mitosis and suggest that the rise contributes to mitotic chromosome condensation by charge neutralization.

Maeshima et al., 2018, Current Biology *28*, 1–8
February 5, 2018
https://doi.org/10.1016/j.cub.2017.12.035

CellPress

Please cite this article in press as: Maeshima et al., A Transient Rise in Free Mg^{2+} Ions Released from ATP-Mg Hydrolysis Contributes to Mitotic Chromosome Condensation, Current Biology (2017), https://doi.org/10.1016/j.cub.2017.12.035

Current Biology
Report

A Transient Rise in Free Mg^{2+} Ions Released from ATP-Mg Hydrolysis Contributes to Mitotic Chromosome Condensation

Kazuhiro Maeshima,[1,7,8,*] Tomoki Matsuda,[2,7] Yutaka Shindo,[3,7] Hiromi Imamura,[4,7] Sachiko Tamura,[1] Ryosuke Imai,[1] Syoji Kawakami,[2] Ryosuke Nagashima,[1] Tomoyoshi Soga,[5] Hiroyuki Noji,[6] Kotaro Oka,[3] and Takeharu Nagai[2,*]
[1]Structural Biology Center, National Institute of Genetics, and Department of Genetics, Sokendai (Graduate University for Advanced Studies), Mishima, Shizuoka 411-8540, Japan
[2]The Institute of Scientific and Industrial Research, Osaka University, Ibaraki, Osaka 567-0047, Japan
[3]Department of Biosciences & Informatics, Keio University, Hiyoshi, Yokohama 223-8522, Japan
[4]Department of Life Science, Kyoto University, Kyoto 606-8501, Japan
[5]Institute for Advanced Biosciences, Keio University, Tsuruoka, Yamagata 997-0052, Japan
[6]Department of Applied Chemistry, The University of Tokyo, Tokyo 113-8656, Japan
[7]These authors contributed equally
[8]Lead Contact
*Correspondence: kmaeshim@nig.ac.jp (K.M.), ng1@sanken.osaka-u.ac.jp (T.N.)
https://doi.org/10.1016/j.cub.2017.12.035

SUMMARY

For cell division, negatively charged chromatin, in which nucleosome fibers (10 nm fibers) are irregularly folded [1–5], must be condensed into chromosomes and segregated. While condensin and other proteins are critical for organizing chromatin into the appropriate chromosome shape [6–17], free divalent cations such as Mg^{2+} and Ca^{2+}, which condense chromatin or chromosomes *in vitro* [18–28], have long been considered important, especially for local condensation, because the nucleosome fiber has a net negative charge and is by itself stretched like "beads on a string" by electrostatic repulsion. For further folding, other positively charged factors are required to decrease the charge and repulsion [29]. However, technical limitations to measure intracellular free divalent cations, but not total cations [30], especially Mg^{2+}, have prevented us from elucidating their function. Here, we developed a Förster resonance energy transfer (FRET)-based Mg^{2+} indicator that monitors free Mg^{2+} dynamics throughout the cell cycle. By combining this indicator with Ca^{2+} [31] and adenosine triphosphate (ATP) [32] indicators, we demonstrate that the levels of free Mg^{2+}, but not Ca^{2+}, increase during mitosis. The Mg^{2+} increase is coupled with a decrease in ATP, which is normally bound to Mg^{2+} in the cell [33]. ATP inhibited Mg^{2+}-dependent chromatin condensation *in vitro*. Chelating Mg^{2+} induced mitotic cell arrest and chromosome decondensation, while ATP reduction had the opposite effect. Our results suggest that ATP-bound Mg^{2+} is released by ATP hydrolysis and contributes to mitotic chromosome condensation with increased rigidity, suggesting a novel regulatory mechanism for higher-order chromatin organization by the intracellular Mg^{2+}-ATP balance.

RESULTS

Development of Förster Resonance Energy Transfer (FRET)-Based Mg^{2+} Indicators to Measure Intracellular Free Mg^{2+}

While Mg^{2+} is the abundant intracellular cation (~10–20 mM) [34, 35], the majority of the Mg^{2+} pool exists in complexes with adenosine triphosphate (ATP) or other molecules, such as proteins [33, 36]; thus, free Mg^{2+} is assumed to be less than 5% of the total cellular Mg^{2+}.

To develop new FRET-based Mg^{2+} indicators, we used the sensor design and principle of the FRET-based Ca^{2+} indicator (Figure 1A), yellow cameleon (YC)3.60 [31], a chimeric protein composed of an enhanced cyan fluorescent protein (ECFP, FRET donor), a Ca^{2+}-binding protein, calmodulin (CaM), a flexible linker, the Ca^{2+}-CaM-binding domain of myosin light chain kinase (M13), and a yellow fluorescent protein (Venus, FRET acceptor). Upon Ca^{2+} binding, CaM rearranges and binds to M13. This conformational change makes ECFP and Venus come together, inducing a drastic increase in FRET efficiency.

We first substituted CaM and M13 in YC3.60 with a cytosolic Mg^{2+}-binding domain from the *Escherichia coli* Mg^{2+} transporter CorA (CorA-CD) [39] (Figure 1A), where Mg^{2+}-dependent conformational change has been suggested [39, 40]. The construct exhibited a small change in the emission ratio, which was determined by dividing the Venus emission by that of ECFP upon light illumination at the ECFP excitation wavelength.

To improve upon this indicator's performance (both in terms of Mg^{2+} affinity and dynamic range), we made the following modifications. First, the N-terminal region of *E. coli* CorA-CD was deleted, because crystal structure data from *Thermotoga maritima* CorA suggest that this region is not involved in Mg^{2+} binding [39, 40]. Second, several amino acids on the putative α6 helix presumably related to Mg^{2+}-dependent structural changes [40]

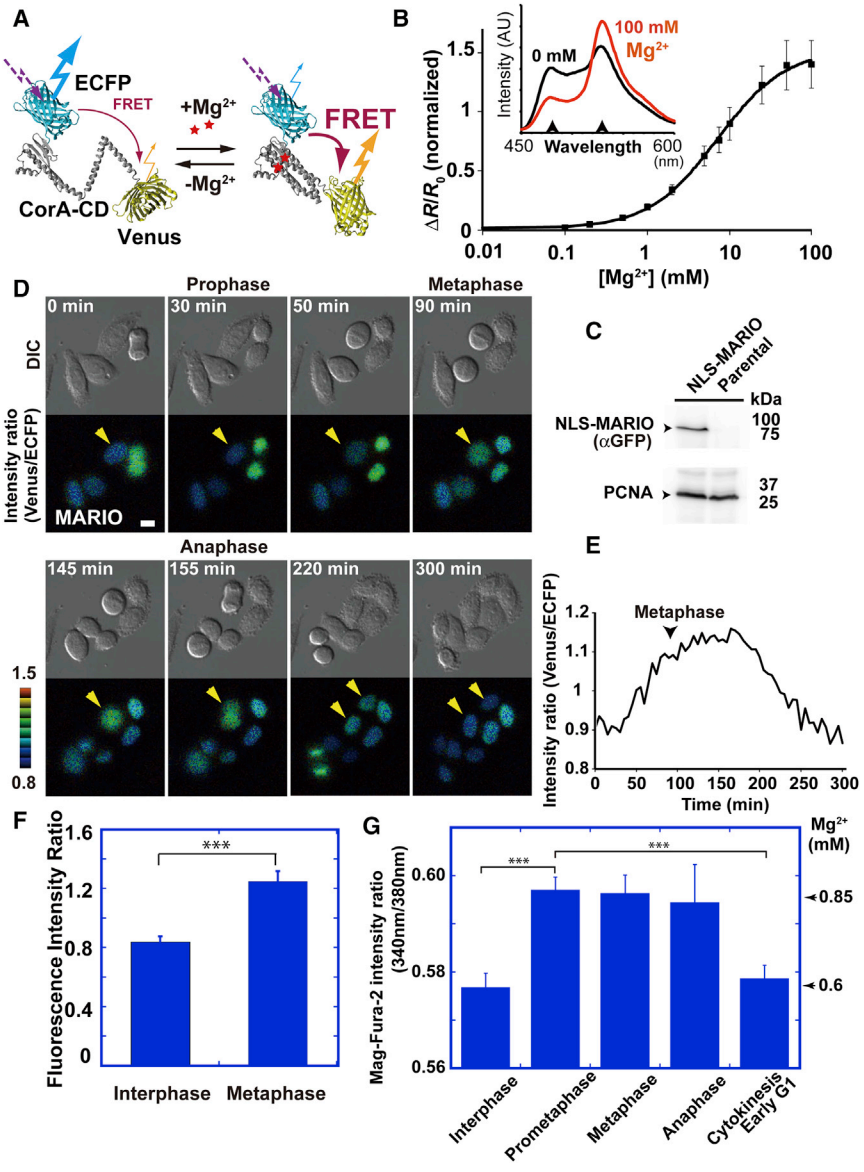

Figure 1. Free Mg^{2+} Measurements during Mitosis

(A) Variants of enhanced cyan fluorescent protein (ECFP) and Venus were connected by a modified cytosolic Mg^{2+}-sensing domain of the *Escherichia coli* Mg^{2+} transporter CorA (CorA-CD). At high Mg^{2+} concentrations (right), increases in the Förster resonance energy transfer (FRET) efficiency between ECFP and Venus were induced via structural changes to CorA-CD. Note that this scheme is highly speculative and is based on available structural data (2YDZ, 1MYW, 3JCG, and 2HN2).

(B) The normalized Venus/ECFP emission ratios of recombinant magnesium ratiometric indicator for optical imaging (MARIO) against the logarithm of Mg^{2+} concentration *in vitro*. Average data from three independent measurements are presented (error bars ± SD). The emission spectra of recombinant MARIO at 0 and 100 mM Mg^{2+} are also shown as an inset.

(C) Efficient expression of NLS-MARIO was confirmed using western blotting (upper). Proliferating cell nuclear antigen (PCNA) was used as a loading control.

(D) Differential interference contrast microscopy (upper, DIC) images and pseudocolored Venus/ECFP emission ratio images (lower, intensity ratio) of MARIO localized in HeLa S3 cell nuclei. Image acquisition began in G2 phase. Elapsed time (in minutes) is shown at the top left. Note that the lower images contain two types of information, color and intensity; the color shows the FRET emission ratio and the intensity reflects the height of the cells. Representative cell images of 54 cells are shown. Scale bar, 10 μm.

(E) Time course of the emission ratio throughout the cell cycle is denoted by the arrowheads in (D). For additional cells, see Figure S1D.

(F) Quantitative analysis of the intensity ratios between interphase (n = 55) and metaphase (n = 45) cells. ***$p < 0.0001$, Welch's t test ($p = 2.2 \times 10^{-16}$).

(G) Mag-Fura-2 [37] was used to confirm the increase in Mg^{2+} during mitosis. The emission ratios were between 340 and 380 nm during each stage of the cell cycle. The estimated Mg^{2+} concentration [38] is depicted by the scale on the right.

Error bars show the SE (n = 288 interphase cells, 298 prometaphase cells, 146 metaphase cells, 40 anaphase cells, and 172 early G1 cells). ***$p < 0.0001$, Student's t test for interphase versus prometaphase ($p = 5.0 \times 10^{-7}$) and Welch's t test for prometaphase versus early G1 phase ($p = 1.7 \times 10^{-6}$). See also Figure S1.

were replaced from polar-charged amino acids to alanine. Finally, we introduced random mutations. In this way, we obtained an indicator with an apparent K_d for Mg^{2+} of 7.2 mM and a dynamic range of 153% (Figures 1A and 1B), which are 49 and 3 times higher than those of MagFRET, respectively [41].

The indicator was named the magnesium ratiometric indicator for optical imaging (MARIO), and its N-terminal region contains 48 amino acid deletions and 4 amino acid mutations (I74D, I184D, K187A, and R189A) compared to *E. coli* CorA-CD. Although MARIO also has affinity for Ca^{2+} (apparent K_d = 6.2 mM) (Figure S1A), this affinity is much lower than the physiological Ca^{2+} range in the cytoplasm (submicromolar concentration; see Figures 2A–2C).

Free Mg^{2+} Increases during Mitosis

To investigate nuclear free Mg^{2+} dynamics during the cell cycle, we attached the nuclear localization signal (NLS) of the SV40 T-antigen to MARIO, which was stably expressed in HeLa S3 cells. The stable expression of NLS-MARIO, with an expected size of ~75 kDa, was confirmed by western blotting (Figure 1C). We monitored nuclear free Mg^{2+} levels throughout the cell cycle. While no notable change in the MARIO emission ratio was observed during interphase (Figures S1B and S1C), after nuclear envelope breakdown (NEBD), the FRET ratio increased and peaked during metaphase when the chromosomes were aligned in the differential interference contrast (DIC) images (Figures 1D and 1E). The ratio gradually decreased during cytokinesis.

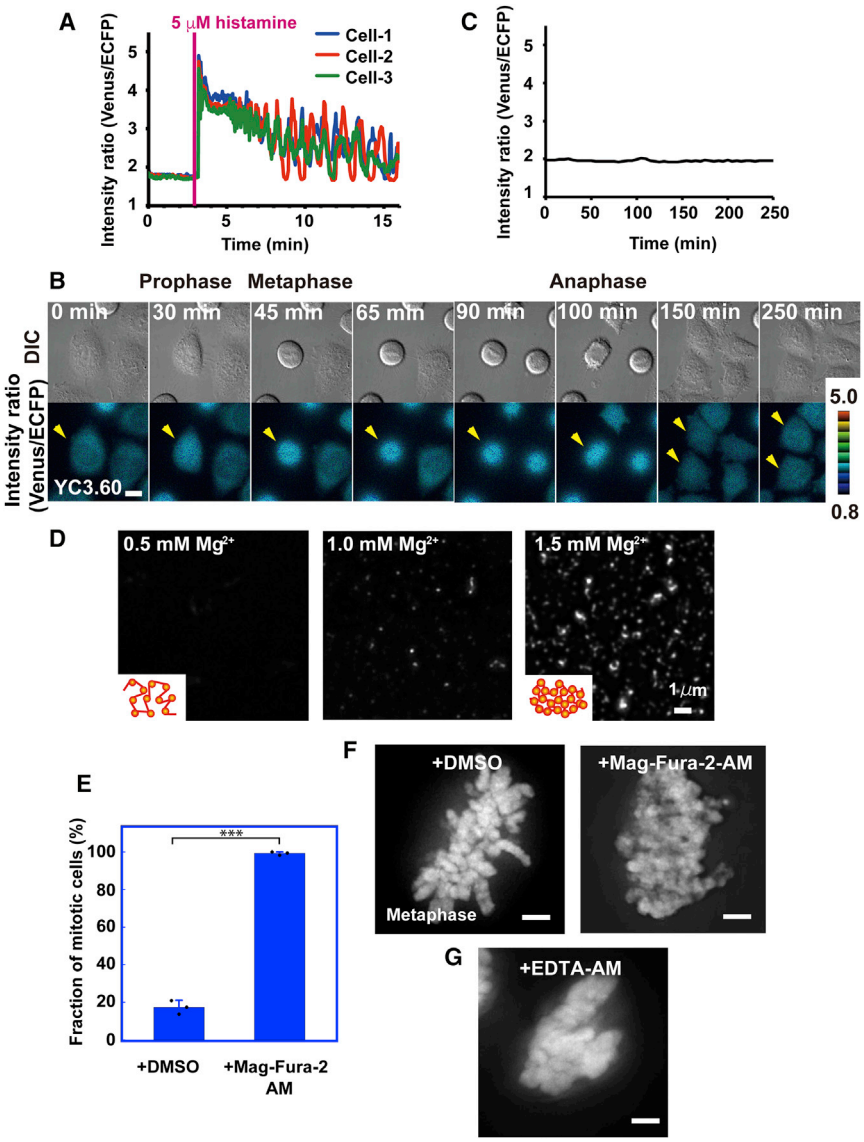

Figure 2. Free Ca^{2+} Measurements during Mitosis

(A) Positive control: emission ratio of YC3.60 expressed in HeLa S3 cells in response to 5 μM histamine stimulation during interphase. The time interval for image acquisition was 3 s. Shown are three representative plots of 36 cells. We estimated that the YC3.60 emission ratios of approximately 1.8 and 5 correspond to 100 nM and 1 μM Ca^{2+}, respectively.

(B) Representative DIC images (upper) and pseudocolored Venus/ECFP emission ratio images of YC3.60 (lower). Image acquisition began in G2 phase. Elapsed time (in min) is shown at the top left. Note that the lower images contain two types of information, color and intensity; the color shows the FRET emission ratio and the intensity reflects the height of the cells. Scale bar, 10 μm.

(C) Time course of the emission ratio throughout the cell cycle is denoted by the arrowheads in (B). Shown is a representative plot of 25 cells.

(D) Condensed chromatin structures at 1.0 and 1.5 mM Mg^{2+} stained with 4',6-diamidino-2-phenylindole (DAPI; right). At 0.5 mM Mg^{2+} (left), no notable structures were observed.

(E) Mitotic retardation of cells treated with Mag-fura2-AM. After treatment with Mag-fura2-AM or dimethyl sulfoxide (DMSO; control) for 80 min, the mitotic fractions were measured. Bars show the SD (n = 3 experiments). ***$p < 0.0001$, Student's t test ($p = 2.9 \times 10^{-6}$).

(F) To investigate the involvement of free Mg^{2+} in the chromosome condensation process, the cell-permeable Mag-Fura2-AM was introduced. The addition of Mag-Fura2-AM induced decondensation of metaphase (right) chromosomes compared to DMSO (control)-treated cells (left).

(G) A similar or even more prominent effect was observed following treatment with ethylenediaminetetraacetic acid, acetoxymethyl ester (EDTA-AM).

See also Figures S2 and S3.

Quantitative analysis demonstrated a significant rise in the free Mg^{2+} level in metaphase-anaphase (Figures 1E, 1F, and S1D). Note that the emission ratios were not affected by changes in the height of the cell or cell shape over the course of the cell cycle. On the other hand, we failed to detect any notable change in the FRET ratio of MagFRET-1 [41] expressed in HeLa S3 cells during mitosis (Figures S1E and S1F), possibly due to its out-of-range K_d for Mg^{2+} and low dynamic range.

To confirm the increase in Mg^{2+} during mitosis, a chemical Mg^{2+} indicator, Mag-Fura-2 (apparent K_d = ~1.9 mM), was employed [37]. Because Mag-Fura-2 accumulates in the cytoplasm and nucleoplasmic Mag-Fura-2 decreases after 2 hr, it could not be used for time-lapse imaging. For Mg^{2+} measurement, mitotic cells were enriched and incubated with the cell-permeable Mag-Fura-2-AM (acetoxymethyl ester; Figure S3A) for 1 hr. This compound can be loaded into cells to generate intracellular Mag-Fura-2. Next, we measured the emission ratios during various stages of the cell cycle, which were categorized based on DIC images. Higher ratios were observed during mitosis, corroborating a significant increase in the free Mg^{2+} level (Figure 1G). To estimate the intracellular concentration of free Mg^{2+}, Mg^{2+} titration using permeabilized cells was performed as described previously [38]. Although we roughly estimated that the Mg^{2+} concentration rose from ~0.6 to ~0.9 mM during mitotic progression (Figure 1G), this value may be underestimated, because chromatin seems to absorb Mg^{2+} and could reduce the FRET ratios of Mag-Fura-2 during the titration (Figure S1H, see legend and also discussed later).

Free Ca^{2+} Levels Do Not Change during Mitosis

Because MARIO shows affinity for another important divalent cation, Ca^{2+} (apparent K_d = 6.2 mM) (Figure S1A), and it was suggested that Ca^{2+} may play a role during mitosis [27, 30], we examined whether free Ca^{2+} increases during mitosis. We measured the concentrations of intracellular free Ca^{2+} via time-lapse imaging with the YC3.60 indicator, an indicator of Ca^{2+}

with a K_d of ~250 nM, which sensitively detects changes in free Ca^{2+} over a large dynamic range of 560% [31]. As a positive control, the upregulation of free Ca^{2+} by histamine stimulation was observed (Figure 2A). From the data available in [42], we estimated that the Ca^{2+} concentration rises from approximately 100 nM to 1 μM upon stimulation with 5 μM histamine, suggesting that YC3.60 emission ratios of ~1.8 and ~5 correspond to 100 nM and 1 μM Ca^{2+}, respectively.

However, in contrast to Mg^{2+} levels, we did not observe any significant change in the intensity ratio for Ca^{2+} during mitosis when the cells became rounded and their chromosomes aligned (Figures 2B and 2C). The emission ratio was around 1.8, and we estimated a nearly constant submicromolar Ca^{2+} concentration throughout mitosis. A similar result (no significant variation in the Ca^{2+} level) was obtained with the conventional chemical Ca^{2+} indicator Fura-2 (Figure S1G) [38]. From these results, we conclude that the levels of free Mg^{2+}, but not Ca^{2+}, increase during mitosis.

Changing the Mg^{2+} Level *In Vivo* Induces Chromatin Condensation *In Vitro*

Next, to ask whether the estimated change in Mg^{2+} level could affect chromatin structure, *in vitro* chromatin condensation assays were performed using purified HeLa S3 chromatin with various concentrations of Mg^{2+} (for a condensation scheme, see Figure S2A). We first employed a differential centrifugation assay [28]; when chromatin condenses due to increased Mg^{2+} concentration, it is recovered in a pellet by microcentrifugation. *In vitro*, condensation occurred dramatically over the range of 0.5 to 1 mM Mg^{2+} (Figure S2B). Condensed chromatin structures ~200 nm in size were visualized by staining with 4',6-diamidino-2-phenylindole (DAPI) in the pellet fraction (Figure 2D). For a more quantitative analysis of chromatin condensation, we performed a static light-scattering assay at 90° [43]. A dramatic condensation effect was observed in the range of ~0.5 to 1 mM Mg^{2+} (Figure S2C), suggesting that this range is important for chromatin structure, consistent with previous reports [18–21, 28]. We also verified that a physiological (submicromolar) concentration of Ca^{2+} did not affect chromatin structure *in vitro* by charge neutralization (Figure S2D).

Chelating Mg^{2+} Induces Mitotic Cell Arrest and Chromosome Decondensation

We tested whether free Mg^{2+} is involved in chromatin condensation during mitosis, as suggested *in vitro*. To this end, we used Mag-Fura-2, which weakly chelates Mg^{2+} (apparent K_d = 1.9 mM) [44] (Figure S3A). Addition of the cell-permeable Mag-Fura-2-AM induced an arrest of mitotic progression (Figure 2E) and chromosome decondensation (Figure 2F). A similar or even more prominent effect was observed following treatment with ethylenediaminetetraacetic acid, acetoxymethyl ester (EDTA-AM) (Figure 2G; for its structure, see Figure S3B). These results support a critical role for Mg^{2+} in chromosome condensation.

ATP, which Captures Mg^{2+} in the Cell, Decreases during Mitosis

Some obvious questions arose from our findings, including where the additional Mg^{2+} originates and how it is regulated during the cell cycle. It is well known that the majority of Mg^{2+} in the cell is coupled with ATP (apparent K_d for Mg^{2+} = 78 μM), which is also abundant in the cell (e.g., ~4 mM in HeLa S3 cells) [33, 35, 45, 46]. To examine ATP cell-cycle dynamics, we used HeLa S3 cells stably expressing the FRET-based ATP indicator ATeam [32], which is composed of the ε subunit of bacterial F_oF_1-ATP synthase sandwiched by ECFP and Venus, with an apparent K_d for ATP of 3.3 mM.

Interestingly, when the cell shape became rounded during NEBD, the emission ratios of Venus to ECFP dropped; then, during anaphase-telophase progression, the emission ratios increased to a higher level than during the previous G2 phase (Figures 3A and 3B). Time-lapse imaging indicated that ATP levels decreased in metaphase-anaphase and recovered during mitotic exit (Figure 3B) and were inversely related to Mg^{2+} (Figures 1D, 1E, and S1D). Considering the average ATP level (~4 mM) in HeLa S3 cells [45] and reported values for the FRET emission ratio reduction rate of ATeam upon complete ATP depletion in the cell [32], we estimated that the reduction of ATP during mitosis is ~1 mM, suggesting that a similar amount of Mg^{2+} (~1 mM) is released, consistent with the possible underestimation by the Mag-Fura-2-based measurement (0.6–0.9 mM; Figures 1G and S1H). Furthermore, luciferase-based ATP measurements showed that synchronized early G1 HeLa S3 cells have ATP levels ~30% higher than mitotic cells (Figure 3C), and this held true in another human cell line (RPE1 [47]) (Figure S3C). Therefore, we propose a novel mechanism by which Mg^{2+} dynamics are regulated during mitosis, in which ATP-bound Mg^{2+} is released by the hydrolysis of ATP.

Because a number of other nucleotides can capture Mg^{2+} ions, we assessed the possible contribution of certain nucleotides and metabolites via metabolomic analysis. Metabolites were recovered from synchronized cells during metaphase and early G1 interphase and then subjected to capillary electrophoresis-based mass spectrometry (CE-MS) [48]. Overall, the CE-MS results support that ATP is a major player in Mg^{2+} capture and that ATP levels decrease in metaphase (Table S1).

ATP Inhibits Mg^{2+}-Dependent Chromatin Condensation *In Vitro*

Next, we asked whether ATP regulates the function of free Mg^{2+}. The isolated human chromosome cluster exhibited a well-condensed morphology with Mg^{2+} (left, Figure 3D). With the addition of 1 mM ATP to Mg^{2+}, the Mg^{2+} effect was neutralized and the chromosomes decondensed (center, Figure 3D; Figure 3E). When ATP treated with calf intestine alkaline phosphatase (CIAP) was used, the decondensation effect was suppressed and the chromosomes remained condensed (right panel of Figure 3D; Figure 3E), with a similar morphology to those given Mg^{2+} only (left panel of Figure 3D; Figure 3E). A more quantitative analysis using the static light scattering of isolated chromatin demonstrated that chromatin condensation by Mg^{2+} was inhibited by ATP (Figures 3F and S3D) and that ATP hydrolysis using CIAP rescued the effects of Mg^{2+} on chromatin condensation (Figures 3F and S3D). The effect of adding adenosine diphosphate (ADP; apparent K_d = ~1 mM) to Mg^{2+} was approximately half that of ATP (Figure S3E). Taken together, we hypothesize that bound Mg^{2+} is released with a decrease in ATP levels and causes further chromosome condensation.

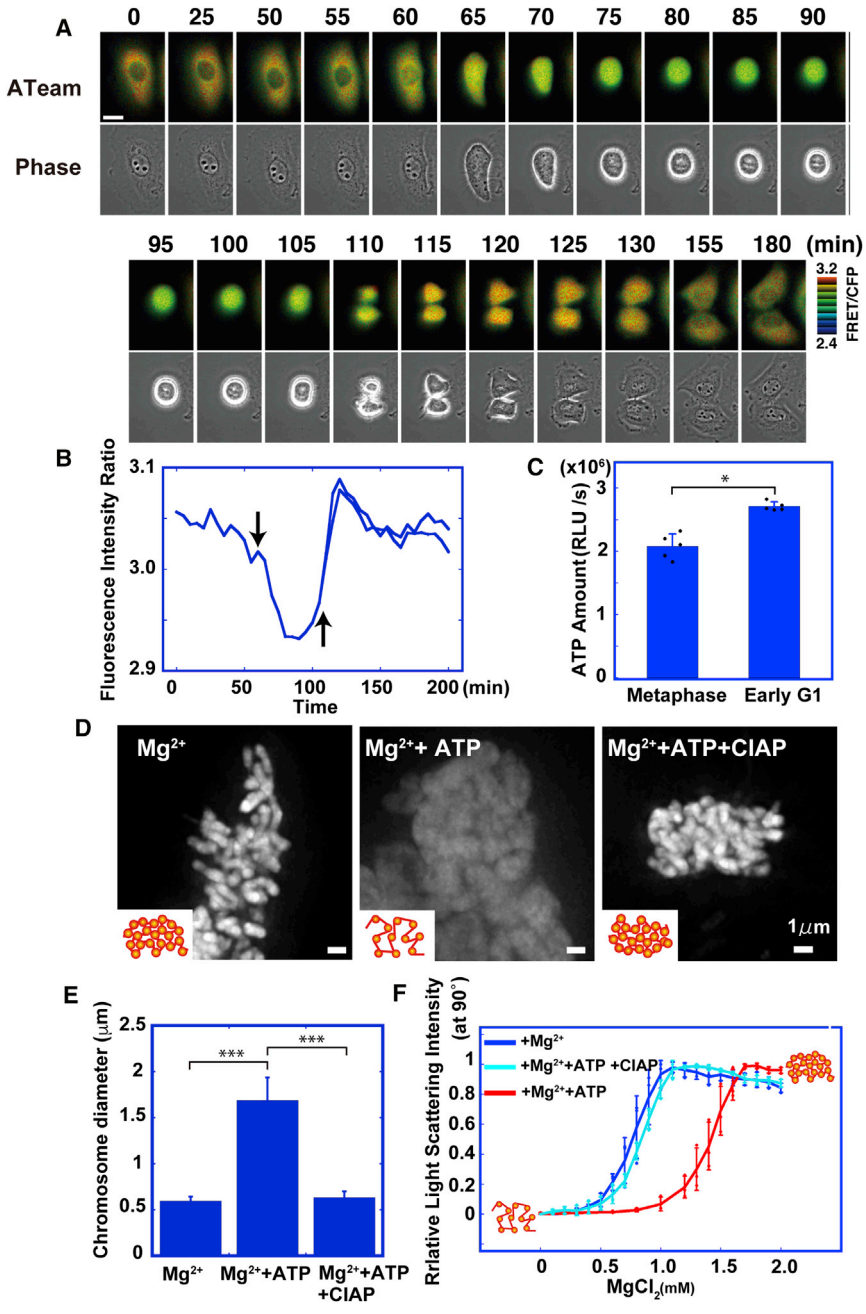

Figure 3. ATP Is Reduced during Mitosis

(A) Time-lapse pseudocolored Venus/ECFP emission intensity ratio images (upper) and phase-contrast images (lower) of ATeam expressed in HeLa S3 cells. Image acquisition began in G2 phase. A representative time-lapse image among eight cells is shown. Elapsed time (in min) is shown at the top. Scale bar, 20 μm.

(B) Time course of the emission ratio in cells indicated in (A). Time points of nuclear envelope breakdown and cytokinesis are indicated by arrows.

(C) Luciferase-based adenosine triphosphate (ATP) measurements for synchronized HeLa S3 cells (0.5×10^5 cells): metaphase cells (left) and early G1 cells (right). Bars represent the SD (n = 5 experiments). *p < 0.01, Student's t test ($p = 1.1 \times 10^{-3}$).

(D) DAPI-stained purified chromosome cluster with 1.5 mM Mg^{2+} (left). Following the addition of 1.5 mM Mg^{2+} and 1 mM ATP, the Mg^{2+} effect diminished and the chromosomes were decondensed (center). The Mg^{2+}-dependent condensation effect reappeared when ATP was hydrolyzed by calf intestine alkaline phosphatase (CIAP) (right).

(E) Quantitative results of chromosome diameter measurement. Bars represent the SD (n = 20 clusters). ***p < 0.0001, Welch's t test ($p = 1.1 \times 10^{-12}$ for both statistical analyses).

(F) A similar set of experiments in (D) was performed using static light-scattering analysis of purified chromatin. Bars represent the SD (n = 3 experiments). This analysis shows that Mg^{2+}-dependent chromatin condensation was inhibited by ATP. With the addition of 1 mM ATP, the rapid increase in intensity occurred at a higher Mg^{2+} level, shifting the curve to the right; however, this effect was not prominent when the ATP added was hydrolyzed by CIAP.

See also Figure S3 and Tables S1 and S2.

Reduced ATP Levels Induce the Hypercondensation of Mitotic Chromosomes

To verify this hypothesis, we reduced the ATP level in mitotic cells by treating them with inhibitors of respiration (NaN_3) and glycolysis (2-deoxyglucose [2DG]). Upon treatment, the MARIO emission ratios in cells increased (Figure S4A). Their DAPI-stained chromosomes had a higher intensity than those of control cells (Figures 4A and 4B) due to the hypercondensation of sister chromatids. This hypercondensation caused by ATP reduction has been reported in another mitotic system [25] as well as in our previous super-resolution imaging of living interphase cells [50]. These results reinforce that ATP-bound Mg^{2+} is released by a decrease in ATP level, which then contributes to chromosome condensation in the cell (Figure 4C). In this situation, ATP acts as a Mg^{2+} reservoir, which might be another function of ATP in addition to being an energy source and a hydrotrope [46].

DISCUSSION

In this study, we demonstrated a transient increase in Mg^{2+} ion concentration, but not Ca^{2+}, during mitosis, which was coupled with a reduction in ATP and facilitated sister chromatid condensation (Figure 4C). Although an increase in the free Ca^{2+} level during mitosis has been reported in several cells, including fish and sea urchin embryogenesis [51–53], the Ca^{2+} concentration after the increase remained around 1 μM, which is too low to induce chromatin condensation *in vitro* (Figure S2D). Therefore, Ca^{2+} may be indirectly involved in the chromatin condensation process by activating protein factors [27, 30] rather than charge neutralization.

Why is further chromosome condensation by Mg^{2+} required for mitosis (Figure 4C)? Since protein factors such as condensin

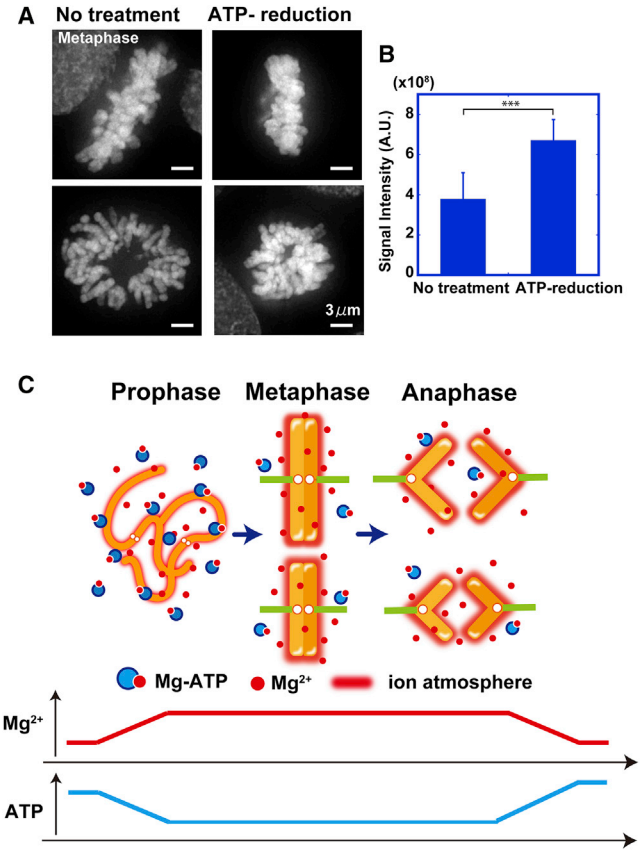

Figure 4. ATP Reduction Induced Hypercondensation of Chromosomes *In Vivo* and a Summary Figure

(A) ATP levels in mitotic cells fell due to treatment with NaN_3 and 2-deoxyglucose, and their chromosomes stained more intensely with DAPI (right) than those of untreated cells.

(B) Quantitative analysis of the integrated DAPI signal intensity of chromosomes suggests the hypercondensation of sister chromatids. Bars represent the SD (n = 20 cells). ***$p < 0.0001$, Student's t test ($p = 7.8 \times 10^{-13}$).

(C) A model. In prophase, the major fraction of Mg^{2+} is bound to ATP. In metaphase, an increase in Mg^{2+}, which is released by the hydrolysis of ATP, contributes to sister chromatid condensation. The "ion atmosphere" sheaths that the cations (including Mg^{2+}) loosely form surrounding chromatin/chromosomes [49] are shown in red. Note that this schematic is highly simplified and not quantitative.

See also Figure S4.

can globally organize mitotic chromosomes [7, 12, 17], we believe that chromosomes become more rigid during the Mg^{2+}-dependent condensation process. This is particularly advantageous for chromosome segregation and transmission during anaphase, which are subject to mechanical shearing stress. Indeed, micro-needle manipulation experiments of isolated chromosomes and nuclei have indicated that chromatin becomes rigid in an Mg^{2+}-dependent manner [54–56]. Our results showed that Mg^{2+} levels remain high during anaphase, consistent with previous reports of anaphase compaction [57, 58].

Regarding ATP dynamics during mitosis, what is the mechanism of reduction? Although one possible mechanism for this ATP reduction is a decrease in the ability to produce energy during mitosis, it seems that neither glycolysis nor oxidative phosphorylation is involved in the ATP reduction process, because glucose uptake in mitotic cells is similar to that in interphase cells (Figure S4B). In addition, our metabolomic analysis indicated that the levels of metabolites related to glycolysis, the tricarboxylic acid (TCA) cycle, and the pentose phosphate pathway are similar in metaphase and early G1 cells (Table S2). The NAD^+/NADH ratios, which reflect both the metabolic activity and health of cells [59], are also comparable between these stages (Table S2).

Another possibility is that an increase in ATP-consuming processes during mitosis reduces the level of ATP. During mitosis, chromosomes are condensed by condensin and other factors and are then dynamically captured, aligned, and segregated by the mitotic spindle apparatus, which all hydrolyze large amounts of ATP. In addition, the phosphorylation of a large number of mitotic proteins, including lamins and histones, is known to occur during mitosis. We estimate that the total ATP consumption for mitotic phosphorylation may reach the submillimolar to millimolar range. Taken together, these coordinated mitotic events may lead to the decrease in ATP level observed during mitosis.

Our study revealed a novel regulatory mechanism for higher-order chromatin organization via the intracellular Mg^{2+}-ATP balance, which is a zero-sum game. A similar regulatory mechanism may work to regulate chromatin organization in other cellular events, such as cell differentiation.

STAR★METHODS

Detailed methods are provided in the online version of this paper and include the following:

- KEY RESOURCES TABLE
- CONTACT FOR REAGENT AND RESOURCE SHARING
- EXPERIMENTAL MODEL AND SUBJECT DETAILS
- METHOD DETAILS
  - DNA construction for the development of MARIO
  - *In vitro* Mg^{2+} and Ca^{2+} titration of MARIO
  - Mg^{2+} imaging by NLS-MARIO in HeLa S3 cells
  - Measurement of intracellular Mg^{2+} concentration using Mag-Fura-2
  - *In vitro* Mg^{2+} titration of Mag-Fura-2
  - ATP imaging in HeLa S3 cells
  - Intracellular ATP measurement based on luciferase activity
  - Chromatin condensation assay using isolated HeLa S3 chromatin and chromosomes
  - Differential centrifugation assay and static light scattering analysis of HeLa S3 chromatin
  - Mag-Fura-2-AM and EDTA-AM treatment of mitotic cells
  - ATP reduction in mitotic cells
  - Metabolomic analysis
  - Glucose uptake assay
- DATA AND SOFTWARE AVAILABILITY

SUPPLEMENTAL INFORMATION

Supplemental Information includes four figures and two tables and can be found with this article online at https://doi.org/10.1016/j.cub.2017.12.035.

ACKNOWLEDGMENTS

We are grateful to Dr. T. Sutani, Dr. D. Hudson, Dr. N. Kleckner, and Dr. G. Guidotti for their critical reading of this manuscript and to Dr. A. Belmont for helpful discussions and support. We thank Dr. K. Horie, Dr. S. Kose, Dr. M. Merkx, and Dr. N. Imamoto for materials; Dr. H. Herrmann, Dr. B. Garcia, and Dr. M. Arita for their valuable advice; and Mr. S. Sakamoto and Ms. K. Igarashi for technical assistance. K.M. is grateful to Dr. U.K. Laemmli for stimulating discussions on Mg^{2+}. This work was supported by a MEXT grant to K.M. (23115005), H.N. (23115002), and T.N. (23115003); a JST CREST grant to K.M. (JPMJCR15G2) and T.N. (JPMJCR15N3); and an AMED-CREST grant to T.S.

AUTHOR CONTRIBUTIONS

K.M., T.N., and K.O. designed the project. T.M., S.K., and T.N. developed MARIO and performed MARIO imaging. Y.S. and K.O. performed Mag-Fura-2 and Fura-2 imaging. H.I. and H.N. performed ATP imaging. S.T. and K.M. performed the chromatin experiments. R.N. and R.I. established NLS-MARIO cells. T.S. performed the metabolomic analysis. K.M., T.M., Y.S., H.I., K.O., and T.N. wrote the manuscript with input from all other authors.

DECLARATION OF INTERESTS

The authors declare no competing interests.

Received: November 2, 2017
Revised: December 12, 2017
Accepted: December 18, 2017
Published: January 18, 2018

REFERENCES

1. Eltsov, M., Maclellan, K.M., Maeshima, K., Frangakis, A.S., and Dubochet, J. (2008). Analysis of cryo-electron microscopy images does not support the existence of 30-nm chromatin fibers in mitotic chromosomes in situ. Proc. Natl. Acad. Sci. USA *105*, 19732–19737.
2. Nishino, Y., Eltsov, M., Joti, Y., Ito, K., Takata, H., Takahashi, Y., Hihara, S., Frangakis, A.S., Imamoto, N., Ishikawa, T., and Maeshima, K. (2012). Human mitotic chromosomes consist predominantly of irregularly folded nucleosome fibres without a 30-nm chromatin structure. EMBO J. *31*, 1644–1653.
3. Fussner, E., Strauss, M., Djuric, U., Li, R., Ahmed, K., Hart, M., Ellis, J., and Bazett-Jones, D.P. (2012). Open and closed domains in the mouse genome are configured as 10-nm chromatin fibres. EMBO Rep. *13*, 992–996.
4. Chen, C., Lim, H.H., Shi, J., Tamura, S., Maeshima, K., Surana, U., and Gan, L. (2016). Budding yeast chromatin is dispersed in a crowded nucleoplasm in vivo. Mol. Biol. Cell *27*, 3357–3368.
5. Ou, H.D., Phan, S., Deerinck, T.J., Thor, A., Ellisman, M.H., and O'Shea, C.C. (2017). ChromEMT: visualizing 3D chromatin structure and compaction in interphase and mitotic cells. Science *357*, eaag0025.
6. Hirano, T. (2012). Condensins: universal organizers of chromosomes with diverse functions. Genes Dev. *26*, 1659–1678.
7. Green, L.C., Kalitsis, P., Chang, T.M., Cipetic, M., Kim, J.H., Marshall, O., Turnbull, L., Whitchurch, C.B., Vagnarelli, P., Samejima, K., et al. (2012). Contrasting roles of condensin I and condensin II in mitotic chromosome formation. J. Cell Sci. *125*, 1591–1604.
8. Maeshima, K., and Laemmli, U.K. (2003). A two-step scaffolding model for mitotic chromosome assembly. Dev. Cell *4*, 467–480.
9. Kireeva, N., Lakonishok, M., Kireev, I., Hirano, T., and Belmont, A.S. (2004). Visualization of early chromosome condensation: a hierarchical folding, axial glue model of chromosome structure. J. Cell Biol. *166*, 775–785.
10. Liang, Z., Zickler, D., Prentiss, M., Chang, F.S., Witz, G., Maeshima, K., and Kleckner, N. (2015). Chromosomes progress to metaphase in multiple discrete steps via global compaction/expansion cycles. Cell *161*, 1124–1137.
11. Nagasaka, K., Hossain, M.J., Roberti, M.J., Ellenberg, J., and Hirota, T. (2016). Sister chromatid resolution is an intrinsic part of chromosome organization in prophase. Nat. Cell Biol. *18*, 692–699.
12. Shintomi, K., Inoue, F., Watanabe, H., Ohsumi, K., Ohsugi, M., and Hirano, T. (2017). Mitotic chromosome assembly despite nucleosome depletion in Xenopus egg extracts. Science *356*, 1284–1287.
13. Samejima, K., Samejima, I., Vagnarelli, P., Ogawa, H., Vargiu, G., Kelly, D.A., de Lima Alves, F., Kerr, A., Green, L.C., Hudson, D.F., et al. (2012). Mitotic chromosomes are compacted laterally by KIF4 and condensin and axially by topoisomerase IIα. J. Cell Biol. *199*, 755–770.
14. Booth, D.G., Takagi, M., Sanchez-Pulido, L., Petfalski, E., Vargiu, G., Samejima, K., Imamoto, N., Ponting, C.P., Tollervey, D., Earnshaw, W.C., and Vagnarelli, P. (2014). Ki-67 is a PP1-interacting protein that organises the mitotic chromosome periphery. eLife *3*, e01641.
15. Cuylen, S., Blaukopf, C., Politi, A.Z., Müller-Reichert, T., Neumann, B., Poser, I., Ellenberg, J., Hyman, A.A., and Gerlich, D.W. (2016). Ki-67 acts as a biological surfactant to disperse mitotic chromosomes. Nature *535*, 308–312.
16. Takagi, M., Natsume, T., Kanemaki, M.T., and Imamoto, N. (2016). Perichromosomal protein Ki67 supports mitotic chromosome architecture. Genes Cells *21*, 1113–1124.
17. Kakui, Y., Rabinowitz, A., Barry, D.J., and Uhlmann, F. (2017). Condensin-mediated remodeling of the mitotic chromatin landscape in fission yeast. Nat. Genet. *49*, 1553–1557.
18. Cole, A. (1967). Chromosome structure. Theor. Biophys. *1*, 305–375.
19. Marsden, M.P., and Laemmli, U.K. (1979). Metaphase chromosome structure: evidence for a radial loop model. Cell *17*, 849–858.
20. Earnshaw, W.C., and Laemmli, U.K. (1983). Architecture of metaphase chromosomes and chromosome scaffolds. J. Cell Biol. *96*, 84–93.
21. Widom, J. (1986). Physicochemical studies of the folding of the 100 A nucleosome filament into the 300 A filament. Cation dependence. J. Mol. Biol. *190*, 411–424.
22. Hudson, D.F., Vagnarelli, P., Gassmann, R., and Earnshaw, W.C. (2003). Condensin is required for nonhistone protein assembly and structural integrity of vertebrate mitotic chromosomes. Dev. Cell *5*, 323–336.
23. Dorigo, B., Schalch, T., Bystricky, K., and Richmond, T.J. (2003). Chromatin fiber folding: requirement for the histone H4 N-terminal tail. J. Mol. Biol. *327*, 85–96.
24. Allahverdi, A., Yang, R., Korolev, N., Fan, Y., Davey, C.A., Liu, C.F., and Nordenskiöld, L. (2011). The effects of histone H4 tail acetylations on cation-induced chromatin folding and self-association. Nucleic Acids Res. *39*, 1680–1691.
25. Visvanathan, A., Ahmed, K., Even-Faitelson, L., Lleres, D., Bazett-Jones, D.P., and Lamond, A.I. (2013). Modulation of Higher Order Chromatin Conformation in Mammalian Cell Nuclei Can Be Mediated by Polyamines and Divalent Cations. PLoS ONE *8*, e67689.
26. Pepenella, S., Murphy, K.J., and Hayes, J.J. (2014). A distinct switch in interactions of the histone H4 tail domain upon salt-dependent folding of nucleosome arrays. J. Biol. Chem. *289*, 27342–27351.
27. Phengchat, R., Takata, H., Morii, K., Inada, N., Murakoshi, H., Uchiyama, S., and Fukui, K. (2016). Calcium ions function as a booster of chromosome condensation. Sci. Rep. *6*, 38281.
28. Maeshima, K., Rogge, R., Tamura, S., Joti, Y., Hikima, T., Szerlong, H., Krause, C., Herman, J., Seidel, E., DeLuca, J., et al. (2016). Nucleosomal arrays self-assemble into supramolecular globular structures lacking 30-nm fibers. EMBO J. *35*, 1115–1132.
29. Maeshima, K., Imai, R., Tamura, S., and Nozaki, T. (2014). Chromatin as dynamic 10-nm fibers. Chromosoma *123*, 225–237.
30. Strick, R., Strissel, P.L., Gavrilov, K., and Levi-Setti, R. (2001). Cation-chromatin binding as shown by ion microscopy is essential for the structural integrity of chromosomes. J. Cell Biol. *155*, 899–910.

31. Nagai, T., Yamada, S., Tominaga, T., Ichikawa, M., and Miyawaki, A. (2004). Expanded dynamic range of fluorescent indicators for Ca(2+) by circularly permuted yellow fluorescent proteins. Proc. Natl. Acad. Sci. USA *101*, 10554–10559.
32. Imamura, H., Nhat, K.P., Togawa, H., Saito, K., Iino, R., Kato-Yamada, Y., Nagai, T., and Noji, H. (2009). Visualization of ATP levels inside single living cells with fluorescence resonance energy transfer-based genetically encoded indicators. Proc. Natl. Acad. Sci. USA *106*, 15651–15656.
33. Grubbs, R.D. (2002). Intracellular magnesium and magnesium buffering. Biometals *15*, 251–259.
34. de Baaij, J.H., Hoenderop, J.G., and Bindels, R.J. (2015). Magnesium in man: implications for health and disease. Physiol. Rev. *95*, 1–46.
35. Romani, A.M. (2011). Cellular magnesium homeostasis. Arch. Biochem. Biophys. *512*, 1–23.
36. Gabriel, T.E., and Günzel, D. (2007). Quantification of Mg2+ extrusion and cytosolic Mg2+-buffering in Xenopus oocytes. Arch. Biochem. Biophys. *458*, 3–15.
37. Raju, B., Murphy, E., Levy, L.A., Hall, R.D., and London, R.E. (1989). A fluorescent indicator for measuring cytosolic free magnesium. Am. J. Physiol. *256*, C540–C548.
38. Grynkiewicz, G., Poenie, M., and Tsien, R.Y. (1985). A new generation of Ca2+ indicators with greatly improved fluorescence properties. J. Biol. Chem. *260*, 3440–3450.
39. Payandeh, J., and Pai, E.F. (2006). A structural basis for Mg2+ homeostasis and the CorA translocation cycle. EMBO J. *25*, 3762–3773.
40. Pfoh, R., Li, A., Chakrabarti, N., Payandeh, J., Pomès, R., and Pai, E.F. (2012). Structural asymmetry in the magnesium channel CorA points to sequential allosteric regulation. Proc. Natl. Acad. Sci. USA *109*, 18809–18814.
41. Lindenburg, L.H., Vinkenborg, J.L., Oortwijn, J., Aper, S.J., and Merkx, M. (2013). MagFRET: the first genetically encoded fluorescent Mg2+ sensor. PLoS ONE *8*, e82009.
42. Zhao, Y., Araki, S., Wu, J., Teramoto, T., Chang, Y.F., Nakano, M., Abdelfattah, A.S., Fujiwara, M., Ishihara, T., Nagai, T., and Campbell, R.E. (2011). An expanded palette of genetically encoded Ca^{2+} indicators. Science *333*, 1888–1891.
43. Dimitrov, S.I., Apostolova, T.M., Makarov, V.L., and Pashev, I.G. (1986). Chromatin superstructure. A study with an immobilized trypsin. FEBS Lett. *200*, 322–326.
44. Shindo, Y., Yamanaka, R., Suzuki, K., Hotta, K., and Oka, K. (2015). Intracellular magnesium level determines cell viability in the MPP(+) model of Parkinson's disease. Biochim. Biophys. Acta *1853*, 3182–3191.
45. Yoshida, T., Kakizuka, A., and Imamura, H. (2016). BTeam, a Novel BRET-based Biosensor for the Accurate Quantification of ATP Concentration within Living Cells. Sci. Rep. *6*, 39618.
46. Patel, A., Malinovska, L., Saha, S., Wang, J., Alberti, S., Krishnan, Y., and Hyman, A.A. (2017). ATP as a biological hydrotrope. Science *356*, 753–756.
47. Bodnar, A.G., Ouellette, M., Frolkis, M., Holt, S.E., Chiu, C.P., Morin, G.B., Harley, C.B., Shay, J.W., Lichtsteiner, S., and Wright, W.E. (1998). Extension of life-span by introduction of telomerase into normal human cells. Science *279*, 349–352.
48. Soga, T., Igarashi, K., Ito, C., Mizobuchi, K., Zimmermann, H.P., and Tomita, M. (2009). Metabolomic profiling of anionic metabolites by capillary electrophoresis mass spectrometry. Anal. Chem. *81*, 6165–6174.
49. Lipfert, J., Doniach, S., Das, R., and Herschlag, D. (2014). Understanding nucleic acid-ion interactions. Annu. Rev. Biochem. *83*, 813–841.
50. Nozaki, T., Imai, R., Tanbo, M., Nagashima, R., Tamura, S., Tani, T., Joti, Y., Tomita, M., Hibino, K., Kanemaki, M.T., et al. (2017). Dynamic organization of chromatin domains revealed by super-resolution live-cell imaging. Mol. Cell *67*, 282–293.
51. Poenie, M., Alderton, J., Tsien, R.Y., and Steinhardt, R.A. (1985). Changes of free calcium levels with stages of the cell division cycle. Nature *315*, 147–149.
52. Kao, J.P., Alderton, J.M., Tsien, R.Y., and Steinhardt, R.A. (1990). Active involvement of Ca2+ in mitotic progression of Swiss 3T3 fibroblasts. J. Cell Biol. *111*, 183–196.
53. Mizuno, H., Sassa, T., Higashijima, S., Okamoto, H., and Miyawaki, A. (2013). Transgenic zebrafish for ratiometric imaging of cytosolic and mitochondrial Ca2+ response in teleost embryo. Cell Calcium *54*, 236–245.
54. Shimamoto, Y., Tamura, S., Masumoto, H., and Maeshima, K. (2017). Nucleosome-nucleosome interactions via histone tails and linker DNA regulate nuclear rigidity. Mol. Biol. Cell *28*, 1580–1589.
55. Poirier, M.G., Monhait, T., and Marko, J.F. (2002). Reversible hypercondensation and decondensation of mitotic chromosomes studied using combined chemical-micromechanical techniques. J. Cell. Biochem. *85*, 422–434.
56. Stephens, A.D., Banigan, E.J., Adam, S.A., Goldman, R.D., and Marko, J.F. (2017). Chromatin and lamin A determine two different mechanical response regimes of the cell nucleus. Mol. Biol. Cell *28*, 1984–1996.
57. Mora-Bermúdez, F., Gerlich, D., and Ellenberg, J. (2007). Maximal chromosome compaction occurs by axial shortening in anaphase and depends on Aurora kinase. Nat. Cell Biol. *9*, 822–831.
58. Kleckner, N., Zickler, D., Jones, G.H., Dekker, J., Padmore, R., Henle, J., and Hutchinson, J. (2004). A mechanical basis for chromosome function. Proc. Natl. Acad. Sci. USA *101*, 12592–12597.
59. Bilan, D.S., and Belousov, V.V. (2016). Genetically encoded probes for NAD+/NADH monitoring. Free Radic. Biol. Med. *100*, 32–42.
60. Maeshima, K., Yahata, K., Sasaki, Y., Nakatomi, R., Tachibana, T., Hashikawa, T., Imamoto, F., and Imamoto, N. (2006). Cell-cycle-dependent dynamics of nuclear pores: pore-free islands and lamins. J. Cell Sci. *119*, 4442–4451.
61. Sawano, A., and Miyawaki, A. (2000). Directed evolution of green fluorescent protein by a new versatile PCR strategy for site-directed and semi-random mutagenesis. Nucleic Acids Res. *28*, E78.
62. Maeshima, K., Iino, H., Hihara, S., Funakoshi, T., Watanabe, A., Nishimura, M., Nakatomi, R., Yahata, K., Imamoto, F., Hashikawa, T., et al. (2010). Nuclear pore formation but not nuclear growth is governed by cyclin-dependent kinases (Cdks) during interphase. Nat. Struct. Mol. Biol. *17*, 1065–1071.
63. Takata, H., Hanafusa, T., Mori, T., Shimura, M., Iida, Y., Ishikawa, K., Yoshikawa, K., Yoshikawa, Y., and Maeshima, K. (2013). Chromatin compaction protects genomic DNA from radiation damage. PLoS ONE *8*, e75622.
64. Ura, K., and Kaneda, Y. (2001). Reconstitution of chromatin in vitro. Methods Mol. Biol. *181*, 309–325.
65. Soga, T., and Heiger, D.N. (2000). Amino acid analysis by capillary electrophoresis electrospray ionization mass spectrometry. Anal. Chem. *72*, 1236–1241.
66. Soga, T., Baran, R., Suematsu, M., Ueno, Y., Ikeda, S., Sakurakawa, T., Kakazu, Y., Ishikawa, T., Robert, M., Nishioka, T., and Tomita, M. (2006). Differential metabolomics reveals ophthalmic acid as an oxidative stress biomarker indicating hepatic glutathione consumption. J. Biol. Chem. *281*, 16768–16776.
67. Yoshioka, K., Takahashi, H., Homma, T., Saito, M., Oh, K.B., Nemoto, Y., and Matsuoka, H. (1996). A novel fluorescent derivative of glucose applicable to the assessment of glucose uptake activity of Escherichia coli. Biochim. Biophys. Acta *1289*, 5–9.

STAR★METHODS

KEY RESOURCES TABLE

REAGENT or RESOURCE	SOURCE	IDENTIFIER
Antibodies		
Rabbit polyclonal anti-GFP	MBL	Cat#598
Rabbit polyclonal anti-human PCNA	Santa Cruz Biotechnology	Cat#sc7907
Bacterial and Virus Strains		
E. coli strain JM109 (DE3)	Promega	P9801
Chemicals, Peptides, and Recombinant Proteins		
Aprotinin	TAKARA	Cat#7290
Empigen BB	Sigma-Aldrich	Cat#45165
Spermine	Sigma-Aldrich	Cat#S1141
Spermidine	Sigma-Aldrich	Cat#S2501
Nocodazole	WAKO	Cat#140-08531
Dimethyl sulfoxide (DMSO)	Sigma-Aldrich	Cat#D2650-5
Albumin (BSA)	Sigma-Aldrich	Cat#A2153
micrococcal nuclease	Worthington	Cat#LS004797
ethylene glycol tetraacetic acid (EGTA)	Funakoshi	Cat#6848
Pfu DNA polymerase	Bio Academia	Cat#02-021
Pfu DNA ligase	Agilent Technologies	Cat#600191
*Dpn*I	New England Biolabs	Cat#R0176S
rTaq DNA polymerase	TAKARA	Cat#R001A
Effectene Transfection Reagent	QIAGEN	Cat#301425
G418	ENZ	Cat#ALX-380-013-G001
Ni-NTA column	QIAGEN	Cat#30230
Mag-Fura-2 acetoxymethyl ester (Mag-Fura-2-AM)	Invitrogen	Cat#M1291
Mag-Fura-2 Tetrapotassium salt	Invitrogen	Cat#M1290
Pluronic F-127	Invitrogen	Cat#P3000MP
digitonin	Sigma-Aldrich	Cat#D141-100MG
phenylmethylsulfonyl fluoride (PMSF)	Sigma-Aldrich	Cat#P7626-1G
Poly-L-lysine	Sigma-Aldrich	Cat#P1524-500MG
Formaldehyde solution	Wako	Cat#064-00406
4',6-diamidino-2-phenylindole (DAPI)	Roche	Cat#10236276001
ethylenediaminetetraacetic acid (EDTA)	Dojindo	Cat#N002
EDTA acetoxymethyl ester (EDTA-AM)	Setareh Biotech	Cat#6145
adenosine triphosphate (ATP)	ORIENTAL YEAST	Cat#45140000
adenosine diphosphate (ADP)	ORIENTAL YEAST	Cat#45120000
calf intestine alkaline phosphatase (CIAP)	TAKARA	Cat#2250A
para-phenylene diamine (PPD)	Sigma-Aldrich	Cat#695106-1G
Sodium azide	Sigma-Aldrich	Cat#S2002-25G
2-deoxy-glucose	Sigma-Aldrich	Cat#D8375-1G
formic acid	Wako	Cat#063-05895
hexakis(2,2-difluoroethoxy)phosphazene	SynQuest	Cat#PN 8H79-3-02
3-aminopyrrolidine	Aldrich	Cat#404624
Fura-2 acetoxymethyl ester (Fura-2-AM)	Invitrogen	Cat#F1221
Histamine Dihydrochloride	Wako Pure Chemical Industries	Cat#085-03554

(*Continued on next page*)

Continued

REAGENT or RESOURCE	SOURCE	IDENTIFIER
Critical Commercial Assays		
Cell ATP Assay reagent	Toyo B-Net	Cat#300–15363
2-NBDG Glucose Uptake Assay Kit	BioVision	Cat#K682-50
Deposited Data		
MARIO	DDBJ	LC316970
Experimental Models: Cell Lines		
Human: HeLa S3	[60]	N/A
Human: HeLa S3 expressing NLS-MARIO	This paper	N/A
Human: HeLa S3 expressing ATeam	This paper	N/A
Human: HeLa S3 expressing YC3.60	[31]	N/A
Human: hTERT RPE1	[47]	N/A
Platinum A retroviral packaging cell line	Cell Biolabs	Cat#RV-102
Oligonucleotides		
Primer: NheI-NLS-Fw, CTAGCTAGCATGGGGG GGCCTCCAAAAAAGAA	This paper	N/A
Primer: SmaI-SV40 pA-Rv, TCCCCCGGGT AAGATACATTGATGAGTTT	This paper	N/A
Primer: CorA-CD-Fw, CCGCATGC ATGCTG AGCGCATTTCAACTG	This paper	N/A
Primer: CorA-CD-Rv, ATGAGCTC AGCCGC CTGCATCAGGAAGTT	This paper	N/A
Primer: CorA-CD-deletion-Fw, CCGCATGCT GAGCCTGGCAACCCGC	This paper	N/A
Primer: CorA-CD-deletion-Rv, ATGAGCTC AGCCGCCTGCATCAGGAAGTT	This paper	N/A
NotI-XhoI linker: a duplex of 5′-GCGGCCGCC-3′ and 5′-TCGAGGCGGCCGC-3′	This paper	N/A
HindIII-BamHI linker: a duplex of 5′-AGCTTGG ATCC-3′ and 5′-GGATCCA-3′	This paper	N/A
Primer: CorA-CD- K187A /R189A, GATATC GGCTGGGCCGTTGCCCTGTGTCTGATG	This paper	N/A
Recombinant DNA		
$pRSET_B$	Invitrogen	Cat#V35120
MARIO/$pRSET_B$	This paper	N/A
pEGFP-C1/T-NLS	Naoko Imamoto Lab. (RIKEN)	N/A
pPB-EF1α-H2B-PA-mCherry-PGKneo	[50]	N/A
pPB-PGKneo-EF1a-NLS-MARIO-SV40 pA	This paper	N/A
pCMV-hyPBase	Kyoji Horie Lab. (Nara Medical Univ.)	N/A
pCMVMagFRET-1	Gifted from Maarten Merkx [41]	Addgene plasmid #50742
pcDNA-AT1.03	[32]	N/A
pQCXIN	Clontech	Cat#631514
Software and Algorithms		
Origin8 software	OriginLab	https://www.originlab.com/index.aspx?go=PRODUCTS/Origin
MetaMorph	Molecular Device	https://www.moleculardevices.com/systems/metamorph-research-imaging/metamorph-microscopy-automation-and-image-analysis-software
Aquacosmos software	Hamamatsu photonics	Installed in Hamamatsu Photonics Fluorescence Imaging system
SoftWoRx software	Applied Precision	Installed in Delta Vision microscope system

CONTACT FOR REAGENT AND RESOURCE SHARING

Further information and requests for resources and reagents should be directed to and will be fulfilled by the Lead Contact, Kazuhiro Maeshima (kmaeshim@nig.ac.jp).

EXPERIMENTAL MODEL AND SUBJECT DETAILS

The cells were cultured in Dulbecco's modified Eagle's medium (DMEM) (Sigma-Aldrich) supplemented with 10% fetal bovine serum (FBS) at 37°C in 5% CO_2.

METHOD DETAILS

DNA construction for the development of MARIO

The gene of a cytosolic domain in the Mg^{2+} transporter CorA was amplified from genomic DNA from *E. coli* using polymerase chain reaction (PCR). A forward primer containing the *Sph*I site and a reverse primer containing the *Sac*I site were used for amplification (5′-CCGCATGC ATGCTGAGCGCATTTCAACTG-3′ and 5′-ATGAGCTC AGCCGCCTGCATCAGGAAGTT-3′). To improve the affinity for Mg^{2+} and the dynamic range of Mg^{2+} concentration, an N-terminal deletion was introduced using PCR with forward primers containing the *Sph*I site followed by methionine and the sequence starting at the 49th residue of CorA (5′-CCGC ATGCTGAGCCTGG CAACCCGC-3′ and 5′-ATGAGCTC AGCCGCCTGCATCAGGAAGTT-3′) [39]. Site-directed mutations (K187A and R189A) were introduced by the modified Quik Change method using one oligonucleotide with mutation sites [61]. Briefly, DNA extension and ligation were simultaneously performed in a mixture containing 1 ng/μL of template plasmid DNA, 1 μM of the 5′ phosphorylated primers to substitute amino acid residues (5′-GATATCGGCTGGGCCGTTGCCCTGTGTCTGATG-3′), 150 μM of dNTPs, 0.1 U/μL of *Pfu* DNA polymerase (Bio Academia), 0.5 × reaction buffer attached to *Pfu* polymerase, 0.08 U/μL of *Pfu* DNA ligase (Agilent Technologies) and 0.5 × reaction buffer attached to *Pfu* ligase. Following the reaction, the template plasmid DNA was eliminated by *Dpn*I (New England Biolabs) digestion. Random mutations were introduced into the CorA cytosolic domain by error-prone PCR with a mixture containing 1 μM of the forward and reverse primers, 1 ng/μL of template plasmid DNA, 0.05 U/μL of rTaq DNA polymerase (TAKARA), 1 × attached reaction buffer, 0.2 mM dATP, 0.2 mM dGTP, 0.9 mM dCTP, 0.9 mM dTTP and 0.4 mM $MnCl_2$.

For protein expression in *E. coli*, the restricted product from MARIO was cloned in-frame into the BamHI/EcoRI sites of $pRSET_B$ (Invitrogen), yielding MARIO/$pRSET_B$.

The construction of NLS-MARIO was carried out as follows. The MARIO fragment was cut out using *Bam*HI/*Eco*RI digestion and blunted. This fragment was inserted into the blunted BamHI site of pEGFP-C1/T-NLS (from the lab of Dr. N. Imamoto). The region containing the *Nhe*I site of NLS-MARIO-SV40 and the pA-SmaI site was amplified via PCR using the following primer set (5′- CTAGC TAGCATGGGGGGGCCTCCAAAAAAGAA-3′, 5′-TCCCCCGGGTAAGATACATTGATGAGTTT-3′). After digestion with *Nhe*I and SmaI, the amplified fragment was inserted into the vector region of pPB-EF1α-H2B-PA-mCherry-PGKneo [50] digested with *Nhe*I and SmaI to obtain pPB-PGKneo-EF1α-NLS-MARIO-SV40 pA. This construct and pCMV-hyPBase (from Dr. K. Horie) were transfected into HeLa S3 cells using Effectene Transfection Reagent (QIAGEN) to create HeLa S3 cells stably expressing NLS-MARIO after selection using 1200 μg/mL of the antibiotic G418.

In vitro Mg^{2+} and Ca^{2+} titration of MARIO

For expression and purification of the MARIO protein, the *E. coli* strain JM109(DE3) transformed with MARIO/$pRSET_B$ was grown for 72 hr at 23°C. The recombinant protein was purified using a Ni-NTA column (QIAGEN), and its emission spectra were measured at a concentration of 0.2 μM using an F-7000 fluorescence spectrophotometer (Hitachi) with 435 nm excitation. Mg^{2+} titrations were performed by reciprocal dilution with Mg^{2+} buffer (50 mM $MgCl_2$) and Mg^{2+}-free buffer containing 25 mM MOPS (pH 7.2) and 100 mM KCl at room temperature (23–25°C). Averaged data from three independent measurements were fitted to the Hill equation in a two-site model using Origin8 software (OriginLab). $CaCl_2$ was used in place of $MgCl_2$ to prepare buffers for Ca^{2+} titration.

Mg^{2+} imaging by NLS-MARIO in HeLa S3 cells

HeLa S3 cells were cultured on a 35 mm glass-bottom dish containing 1.5 mL FluoroBrite DMEM (Thermo Fisher Scientific) supplemented with 10% FBS and imaged with a widefield inverted epifluorescence microscope (Ti-E, Nikon) equipped with a 40 × oil immersion objective (Plan Fluor, numerical aperture [NA] 1.3; Nikon). The samples were illuminated with a 100 W mercury arc lamp through 5%, 12.5%, and 25% neutral density filters and a 434/17 excitation filter (Semrock). The cyan and yellow fluorescence signals were sequentially captured through 483/32 and 542/27 interference filters (Semrock), respectively, using an emission filter changer (Ludl Electronic Products). An electron-multiplying charge-coupled device (EMCCD) camera (iXon3, Andor Technology) was used to acquire images with 2 × 2 binning, with an exposure time of 500 ms and an EM gain of 500 for each channel. During time-lapse imaging, dishes were incubated in a microscope incubator (Tokai Hit) with 5% CO_2 at 37°C. After background subtraction, a ratio image was created based on the yellow and cyan fluorescent protein filters (YFP/CFP) using Intensity Modulated Display mode (IMD) of MetaMorph software (Molecular Devices). Time-lapse images of cell mitosis were captured every 5 min. Although the apparent K_d of MARIO 7.2 mM is not close to the nuclear free Mg^{2+} concentration, MARIO with a dynamic range of 153% was sensitive enough to detect the Mg^{2+} fluctuation (~0.6 to ~0.9 mM) during the cell cycle. Note that the images are presented without

contrast enhancement. Time-lapse Mg^{2+} imaging during cell mitosis with MagFRET-1 was performed under the same conditions except for an EM gain of 200 for each channel. HeLa S3 cells transfected with pCMVMagFRET-1 gifted from Maarten Merkx (Addgene plasmid #50742) [41] were used for imaging.

We performed Ca^{2+} imaging by YC3.60 in HeLa S3 cells as described above, except that the EM gain was 200. For time-lapse imaging of histamine-dependent changes in Ca^{2+}, 15 μL of 500 μM histamine dissolved in medium was added so that the final concentration was 5 μM. Images were captured every 3 s.

Measurement of intracellular Mg^{2+} concentration using Mag-Fura-2

Mag-Fura-2-AM (Invitrogen) was applied to the culture medium at 10 μM with 0.02% Pluronic F-127 (Invitrogen), and the cells were incubated at 37°C for 30 min. The cells were then washed twice with Hank's balanced salt saline (HBSS, pH adjusted to 7.4; Invitrogen) and further incubated in fresh HBSS at 37°C for 15 min to complete hydrolysis of the acetoxymethyl (AM) ester form.

Mag-Fura-2 fluorescence was measured on a fluorescence microscope (ECLIPSE TE300, Nikon) equipped with a 10 × objective lens (S Fluor, Nikon). Mag-Fura-2 was alternately excited at 340 nm (Mg^{2+}-bound) and 380 nm (Mg^{2+}-unbound) using a 150 W Xe lamp fitted with a monochromator. Fluorescence was detected with a CCD camera (HiSCA, Hamamatsu Photonics) through a 400 nm dichroic mirror and a 535/55 nm emission filter (Nikon). Fluorescence was quantitatively analyzed using Aquacosmos software (Hamamatsu Photonics), and fluorescence intensity was calculated as the mean intensity in the region of interest (ROI), which contained the entire cell body. To measure the changes in Ca^{2+}, fura-2-AM (Invitrogen) was used as described above.

The Mg^{2+} concentration was calibrated using the emission ratio of Mag-Fura-2 following a previously published method [38]: To estimate R_{max} and R_{min}, HeLa cells were incubated in high-Mg^{2+} medium (100 mM Mg^{2+}) or in Mg^{2+}-free medium (0 mM Mg^{2+}) for 10 min with 0.00125% digitonin. The digitonin was washed out, and the cells were further incubated in the medium for an additional 30 min. The cells were stained with Mag-Fura-2 and their fluorescence was measured in the incubation medium. Although we took great effort to estimate the intracellular Mg^{2+} concentrations by MARIO, we were unsuccessful. When Mg^{2+} was introduced into cells, MARIO behaved abnormally, possibly because the MARIO protein may become insoluble or form aggregates with chromatin. We thus used Mag-Fura-2 for the estimation.

In vitro Mg^{2+} titration of Mag-Fura-2

The fluorescence intensity of Mag-Fura-2 was measured at a concentration of 10 μM (10 mM HEPES and 0.1 mM EDTA) on a plate reader (VARIOSKAN Flash, Thermo Fisher Scientific). Titration was performed in $MgCl_2$ (ranging from 0 to 2 mM). The fluorescence intensities at 510 nm (excited at 340 and 380 nm) were measured and their ratio was calculated. The same sets of experiments were also performed with 100 μg/mL chromatin or albumin.

ATP imaging in HeLa S3 cells

To express ATeam in HeLa S3 cells, an *Xho*I-*Hind*III DNA fragment encoding ATeam from pcDNA-AT1.03 [32] was ligated between the *Not*I and BamHI sites of pQCXIN (Clontech Laboratories) using a *Not*I-*Xho*I linker (a duplex of 5′-GCGGCCGCC-3′ and 5′-TCGAGGCGGCCGC-3′) and a *Hind*III-BamHI linker (a duplex of 5′-AGCTTGGATCC-3′ and 5′-GGATCCA-3′) to obtain pQCXIN-AT1.03. Retroviral particles, which were produced by lipofection of the Platinum-A retroviral packaging cell line (Cell Biolabs) with pQCXIN-AT1.03, were used to obtain a HeLa S3 cell line stably expressing ATeam.

To image ATP in HeLa S3 cells expressing ATeam [32], cells were cultured on a 35 mm glass-bottom dish containing 2 mL phenol-red-free DMEM (low glucose) supplemented with 10% FBS and imaged with a widefield inverted epifluorescence microscope (Ti-E, Nikon) equipped with a 40 × dry objective (Plan Apo, numerical aperture 0.95; Nikon). The samples were illuminated with a 75 W xenon arc lamp through 12.5% and 25% neutral density filters and a 438/24 excitation filter (Semrock). The cyan and yellow fluorescence signals were sequentially captured through 483/32 and 542/27 interference filters (Semrock), respectively, using an emission filter changer (Nikon). An sCMOS camera (Zyla 4.2, Andor Technology) was used to acquire images. During time-lapse imaging, dishes were incubated in a microscope stage top incubator (Tokai Hit) with 5% CO_2 at 37°C. Time-lapse images of cell mitosis were captured every 5 min. After background subtraction, YFP/CFP ratio images were created using MetaMorph software (Molecular Devices).

Intracellular ATP measurement based on luciferase activity

To initiate cell synchronization, mitotic shake-off was performed using HeLa S3 cells treated with 0.1 μg/mL Nocodazole (Wako) for 4 hr [62]. Aliquots of 0.5×10^5 mitotic cells were seeded into a 12-well culture plate (IWAKI) and cultured for 40 min (metaphase) or 4 hr (early G1). To measure ATP, Cell ATP Assay Reagent (300–15363, Toyo B-Net) was used according to the manufacturer's instructions. Bioluminescence was measured using a Lumat LB 9507 tube luminometer (EG&G BERTHOLD). A standard plot of ATP concentration versus bioluminescence intensity validated that our measured ATP concentration values were within a linear range. Both the reaction and measurement were performed at 23°C in the dark. The incubation time from the addition of the assay reagent to measurement was 5 min. ATP measurement of RPE1 cells was performed as described above.

Chromatin condensation assay using isolated HeLa S3 chromatin and chromosomes

HeLa S3 nuclear isolation was performed as described previously [63]. Briefly collected cells were suspended in nuclei isolation buffer (3.75 mM Tris-HCl [pH 7.5], 20 mM KCl, 0.5 mM EDTA, 0.05 mM spermine (Sigma-Aldrich), 0.125 mM spermidine (Sigma-Aldrich), 1 μg/mL Aprotinin (Takara), 0.1 mM phenylmethylsulphonyl fluoride [PMSF] [Sigma-Aldrich]) and centrifuged at 1936 × *g*

for 7 min at room temperature. The cell pellets were resuspended in nuclei isolation buffer and again centrifuged at 1936 × *g* for 7 min at room temperature. The cell pellets were then resuspended in nuclei isolation buffer containing 0.025% Empigen (Sigma-Aldrich) (nuclei isolation buffer+) and homogenized immediately with ten downward strokes using a tight Dounce-pestle (Wheaton). The cell lysates were centrifuged at 4336 × *g* for 5 min. The nuclei pellets were washed in nuclei isolation buffer+. Next, chromatin isolation was carried out as described by Ura and Kaneda [64] with slight modifications. Nuclei (equivalent to ~2 mg DNA) were digested in nuclear isolation buffer (10 mM Tris-HCl, pH 7.5, 1.5 mM $MgCl_2$, 1.0 mM $CaCl_2$, 0.25 M sucrose, and 0.1 mM PMSF) with 50 units of micrococcal nuclease (Worthington) at 35°C for 2 min. The reaction was stopped by adding EGTA to a final concentration of 2 mM. After washing with nuclear isolation buffer, the nuclei were lysed with lysis buffer (10 mM Tris-HCl, pH 7.5, 5 mM EDTA, and 0.1 mM PMSF). The lysate was dialyzed against dialysis buffer (10 mM Tris-HCl, pH 7.5, 0.1 mM EDTA, and 0.1 mM PMSF) at 4°C overnight. The dialyzed lysate was centrifuged at 1000 × *g* at 4°C, and the supernatant was recovered and used as the purified chromatin fraction.

Samples (2 μg) of HeLa S3 chromatin were incubated with various concentrations of $MgCl_2$ and ATP for 15 min on ice and spun onto poly L-lysine-coated coverslips by centrifugation at 2380 × *g* for 15 min. For the chromosome condensation assay, the chromosome clusters included in the purified nuclear fraction [63] were used following the procedure described above. The chromatin and chromosomes were gently fixed with 2% formaldehyde (Wako) in the same buffer. After DNA staining with DAPI, the coverslips were sealed with nail polish. Optical sectioning images were recorded with a 200 nm step size using a DeltaVision microscope (Applied Precision) and deconvolved to remove out-of-focus information. Projected images from five sections are shown.

Differential centrifugation assay and static light scattering analysis of HeLa S3 chromatin

HeLa S3 chromatin was diluted to 100 μg/mL in buffer containing 10 mM HEPES (pH 7.5) and 0.1 mM EDTA, and then subjected to a differential centrifugation assay as described previously [28]. Briefly, $MgCl_2$ was added to the chromatin solution at the indicated concentration and the suspension was centrifuged at 5800 × *g* for 5 min at 4°C. How much fraction of chromatin was recovered in the supernatant was measured by OD260 with NanoDrop1000 Spectrophotometer (Thermo Fisher Scientific).

To analyze static light scattering by HeLa S3 chromatin, diluted HeLa S3 chromatin was centrifuged at 15,000 rpm for 1 min, and 200 μL supernatant was used for analysis. Static light scattering at 90° was measured using a fluorescence spectrophotometer (F-4500, Hitachi) at a wavelength of 350 nm. For Mg^{2+} or Ca^{2+} titration, a 10 mM solution of $MgCl_2$ or $CaCl_2$ was added to the samples to obtain the desired final concentration. The value measured at 0 mM was subtracted from all other measurements as background. After background subtraction, the resultant values were normalized to the peak value. The mean values from triplicate experiments were plotted with their standard deviations. To test the effects of ATP, Mg^{2+} titration was performed with 1 mM ATP. To hydrolyze ATP, 100 μL of 50 mM ATP solution was treated with 90 units of CIAP (Takara) at 37°C for 30 min, followed by 15 min of heat inactivation at 65°C, and used for measurement at a final concentration of 1 mM.

Mag-Fura-2-AM and EDTA-AM treatment of mitotic cells

HeLa S3 mitotic cells were collected by the mitotic shake-off method [62] and seeded onto a 12-well culture plate (IWAKI) with and without poly lysine-coated coverslips containing DMEM (Life Sciences) supplemented with 10% FBS. Mag-Fura-2-AM (Invitrogen), which was dissolved in DMSO at 40 mM, was added to the culture medium at a final concentration of 25 μM with 0.02% Pluronic F-127 (Invitrogen), and the cells were further incubated at 37°C for 80 min. For control cells, the same amounts of DMSO and F-127 were used. After incubation for 80 min, the numbers of mitotic cells and interphase cells were counted. The cells on the coverslips were fixed, stained with DAPI, and mounted with para-phenylene diamine (PPDI) solution (20 mM HEPES, pH 7.4, 1 mM $MgCl_2$, 100 mM KCl, 78% glycerol, 1 mg/mL PPDI[Sigma-Aldrich]) [60]. Cell images were recorded with a DeltaVision microscope (Applied Precision) following a published protocol [28]. In the case of EDTA, tetra(acetoxymethyl ester) (EDTA-AM) (6145, Setareh Biotech), which was dissolved in 100 mM DMSO, EDTA-AM was added to the culture medium at a final concentration of 20 μM with 0.02% Pluronic F-127 (Invitrogen), and the cells were further incubated at 37°C for 100 min.

ATP reduction in mitotic cells

HeLa S3 cells were grown on poly lysine-coated coverslips in a 12-well culture plate (IWAKI) containing DMEM (Life Sciences) supplemented with 10% FBS. For ATP reduction, the cells were incubated on coverslips with 10 mM sodium azide and 50 mM 2-deoxyglucose in HBSS (GIBCO) for 10 min. The treated and non-treated cells were fixed, stained with DAPI, and mounted with PPDI described above [60]. Cell images were recorded with a DeltaVision microscope (Applied Precision) [28]. Because the diameter of hypercondensed chromosomes is difficult to measure, the average DAPI intensity in chromosome cluster regions of the images was quantified without deconvolution by SoftWoRx software with a certain threshold value. n = 12 (ATP reduction) and 8 (control) cells. To evaluate Mg^{2+} levels under normal and ATP-reduction conditions, DIC images and emission ratio images (lower, intensity ratio) of MARIO expressed in asynchronous HeLa S3 cells were obtained. The average ratios were then calculated. n = 55 cells for each condition.

Metabolomic analysis

HeLa S3 mitotic cells (2×10^6 cells) were collected by the mitotic shake-off method [62] and seeded onto a poly lysine-coated culture dish (IWAKI) containing DMEM (Life Sciences) supplemented with 10% FBS, and analyzed 1 hr (mitotic cells) and 4 hr (early G1 cells) late. The concentrations of all charged metabolites in the samples were measured using capillary electrophoresis time-of-flight mass

spectrometry (CE-TOFMS) (Agilent Technologies) previously developed by the authors of the present study [48, 65]. Briefly, we analyzed cationic compounds using a fused silica capillary (50 μm i.d. × 100 cm) with 1 M formic acid as the electrolyte [65]. Methanol/water (50% v/v) containing 0.1 μM hexakis(2,2-difluoroethoxy)phosphazene was delivered as the sheath fluid at 10 μL/min. Electrospray ionization (ESI)-TOFMS was performed in positive ion mode with the capillary voltage set to 4 kV. Automatic recalibration of each acquired spectrum was performed based on the masses of the reference standards ([13C isotopic ion of a protonated methanol dimer (2 MeOH+H)]+, m/z 66.0632 and [hexakis(2,2-difluoroethoxy)phosphazene +H]+, m/z 622.0290). To identify metabolites, relative migration times were calculated for all peaks by normalization to the reference compound, 3-aminopyrrolidine. Metabolites were identified by comparison of their m/z values and relative migration times to those of the metabolite standards and quantified by comparison of their peak areas to calibration curves generated using methionine sulfone internal standards. Analysis conditions were identical to those described [66].

To analyze anionic metabolites, a commercially available COSMO(+) (chemically coated with cationic polymer) capillary (50 μm i.d. × 105 cm) (Nacalai Tesque) was used with 50 mM ammonium acetate solution (pH 8.5) as the electrolyte. Methanol/5 mM ammonium acetate (50% v/v) containing 0.1 μM hexakis(2,2-difluoroethoxy)phosphazene was delivered as the sheath fluid at 10 μL/min. ESI-TOFMS was performed in negative ion mode, and the capillary voltage was set to 3.5 kV. For anion analysis, trimesate and CAS were used as the reference compound and internal standard, respectively. All other conditions were identical to those described [48].

Glucose uptake assay

An uptake assay of the fluorescent glucose analog (2-NBDG2-deoxy-2-[(7-nitro-2,1,3-benzoxadiazol-4-yl)amino]-D-glucose) [67] was performed using the 2-NBDG Glucose Uptake Assay Kit (K682-50, BioVision) according to the manufacturer's instructions.

DATA AND SOFTWARE AVAILABILITY

Data that support the findings of this study are available from the corresponding author upon request.

Current Biology, Volume *28*

Supplemental Information

A Transient Rise in Free Mg^{2+} Ions Released from ATP-Mg Hydrolysis Contributes to Mitotic Chromosome Condensation

Kazuhiro Maeshima, Tomoki Matsuda, Yutaka Shindo, Hiromi Imamura, Sachiko Tamura, Ryosuke Imai, Syoji Kawakami, Ryosuke Nagashima, Tomoyoshi Soga, Hiroyuki Noji, Kotaro Oka, and Takeharu Nagai

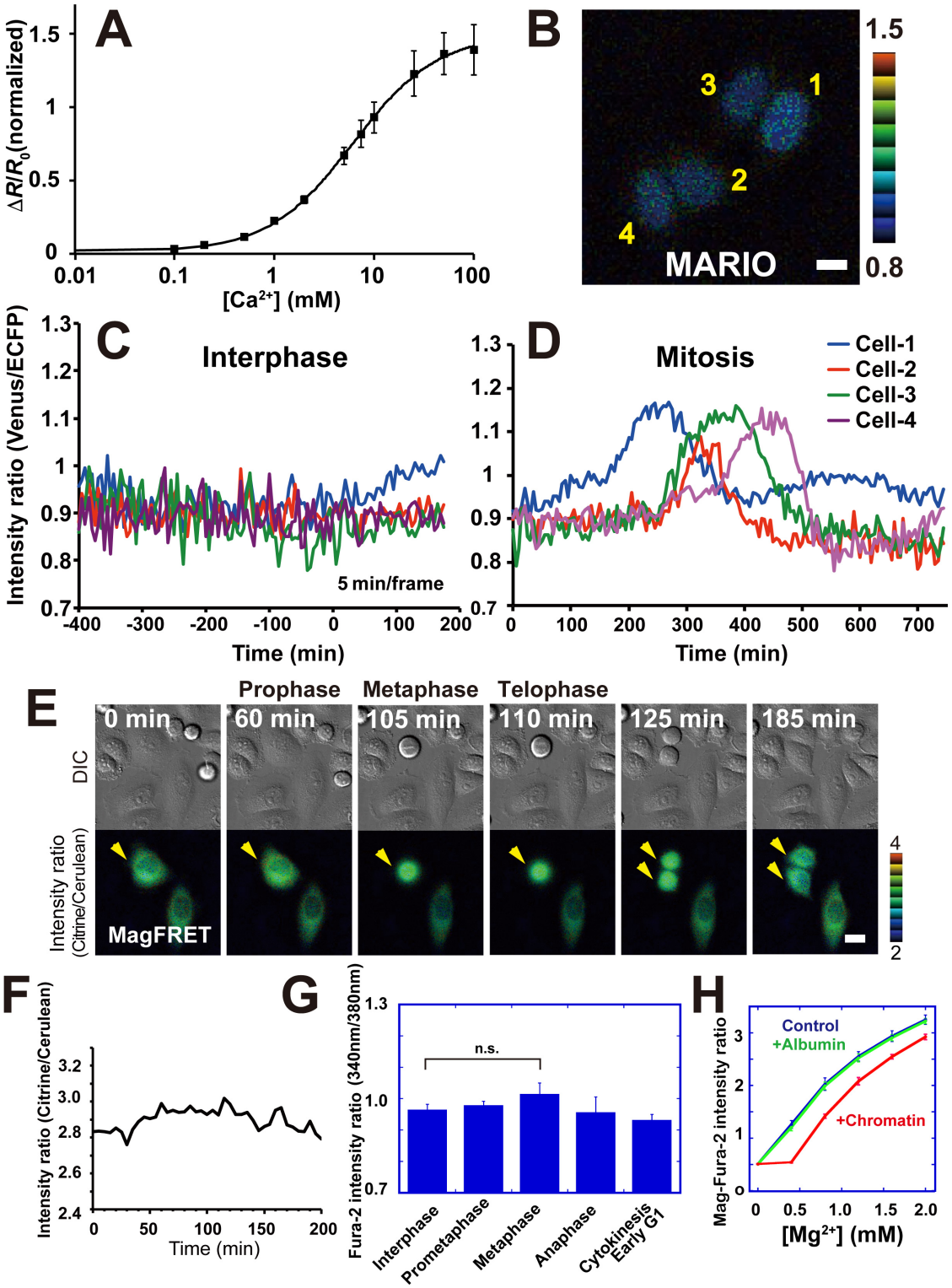
A
ΔR/R0 (normalized)
[Ca2+] (mM)
B
MARIO
1.5
0.8
C
Interphase
Intensity ratio (Venus/ECFP)
5 min/frame
Time (min)
D
Mitosis
Cell-1
Cell-2
Cell-3
Cell-4
Time (min)
E
Prophase
Metaphase
Telophase
0 min
60 min
105 min
110 min
125 min
185 min
DIC
Intensity ratio (Citrine/Cerulean)
MagFRET
F
Intensity ratio (Citrine/Cerulean)
Time (min)
G
Fura-2 intensity ratio (340nm/380nm)
n.s.
Interphase
Prometaphase
Metaphase
Anaphase
Cytokinesis Early G1
H
Mag-Fura-2 intensity ratio
Control
+Albumin
+Chromatin
[Mg2+] (mM)

Figure S1

Figure S1, related to Figure 1.

(A) The Förster resonance energy transfer (FRET) emission ratio of recombinant Magnesium Ratiometric Indicator for Optical imaging (MARIO) was plotted against the logarithm of Ca^{2+} concentration *in vitro*. Data represent the averages from three independent measurements (error bars ± standard deviation). **(B)** Pseudocolored Venus/ enhanced cyan fluorescent protein (ECFP) emission ratio image from the first frame of the time-lapse imaging of four representative HeLa S3 cells (same set as in Figure 1D) in G2 phase. Scale bar, 10 μm. **(C** and **D)** Time course of the emission ratio before (C) and during (D) mitosis in the cells numbered in Figure S1B and also shown in Figure 1D. Note that an increase in the intensity ratio was observed only during mitosis. Four representative profiles of the 54 examined cells are presented. **(E)** Differential interference contrast microscopy (upper, DIC) images and pseudocolored Citrine/Cerulean emission ratio images (lower, intensity ratio) of MagFRET-1 expressed in HeLa S3 cells. Image acquisition began in G2 phase. Elapsed time (in min) is shown at the top left. Note that the lower images contain two types of information, color and intensity; the color shows the FRET emission ratio and the intensity reflects the height of the cells. Representative cell images among 14 cells, which did not show a similar intensity peak to MARIO during the mitotic period, are shown. Scale bar, 20 μm. **(F)** Time course of the emission intensity ratio throughout the cell cycle is denoted by the arrowheads in (E). **(G)** The Ca^{2+} indicator Fura-2 (apparent K_d = 224 nM) [S1] was used to confirm the Ca^{2+} level during mitosis. The intensity ratio between 340 and 380 nm during each stage of the cell cycle is presented. Error bars show the standard error. n = 97 interphase cells, 64 prometaphase cells, 32 metaphase cells, 20 anaphase cells, and 24 early G1 cells. n.s., not significant, Student's *t*-test (p = 0.17). **(H)** *In vitro* Mg^{2+} titration of Mag-Fura-2 with (red line) or without (blue and green lines) chromatin. Titration was performed under an $MgCl_2$ range from 0 to 2 mM, and Mag-Fura-2 intensity ratios are shown (blue line, control). With the addition of 100 μg/mL chromatin, the ratios decreased (red line), but not with albumin (green line), suggesting that chromatin absorbed Mg^{2+} and reduced Mag-Fura-2 ratios during the titration. n = 3 experiments. Bars represent the standard deviation.

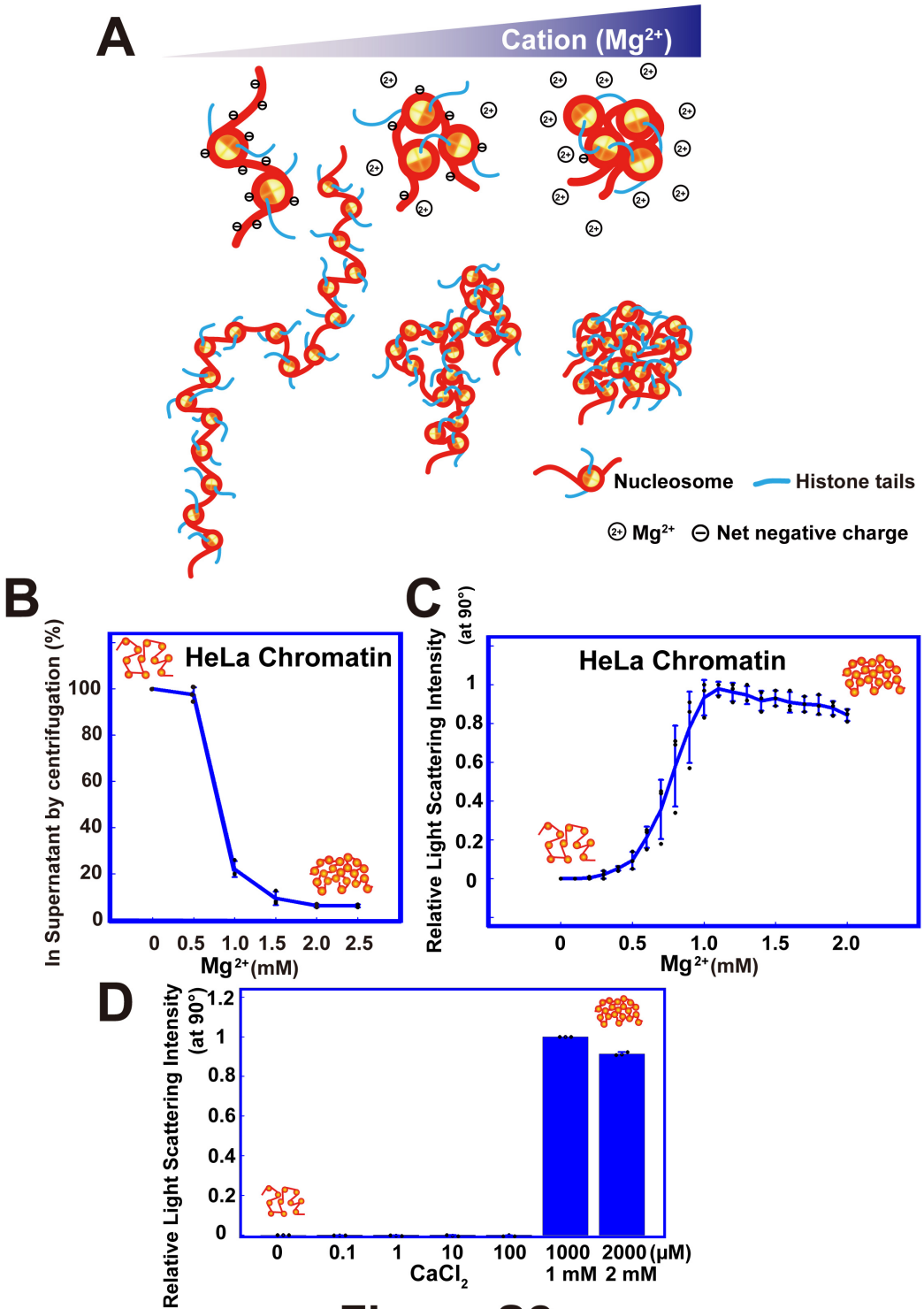
A
Cation (Mg2+)
Nucleosome
Histone tails
Mg2+
Net negative charge
B
HeLa Chromatin
In Supernatant by centrifugation (%)
Mg2+(mM)
C
HeLa Chromatin
Relative Light Scattering Intensity (at 90°)
Mg2+(mM)
D
Relative Light Scattering Intensity (at 90°)
CaCl2
1 mM
2 mM

Figure S2

Figure S2, related to Figure 2.

(A) A schematic for cation-dependent chromatin condensation. In the absence of cations and factors, the chromatin is stretched by electrostatic repulsion (left). In the presence of Mg^{2+}, Mg^{2+} is weakly associated with the phosphate backbone of DNA in chromatin (*i.e.*, ion atmosphere in Figure 4C [S2]), and then decreases its net negative charge and repulsion (center). In this situation, nucleosome–nucleosome interactions via histone tails in the chromatin increase and dominate the repulsion, leading to local chromatin folding (center). More Mg^{2+} can almost completely eliminate the repulsion and promote interdigitated nucleosome–nucleosome interactions via histone tails and the assembly of higher order structures, such as chromatin domains or mitotic chromosomes (right). **(B)** Differential centrifugation assay of isolated HeLa S3 chromatin [S3]. Bars represent the standard deviation (n = 3 experiments). Note that HeLa S3 chromatin was soluble in 0.5 mM Mg^{2+} and mostly pelleted in 1 mM Mg^{2+}. **(C)** Mg^{2+}-dependent chromatin condensation observed by static light scattering analysis at 90° [S4]. Relative scattering intensity values at the indicated Mg^{2+} concentrations are shown. Bars indicate the standard deviation (n = 3 experiments). A sharp increase in intensity was observed from 0.5 to 1 mM Mg^{2+}. **(D)** Chromatin condensation assay at various concentrations of Ca^{2+} was performed using the static light scattering method. Relative scattering intensity values at the indicated Ca^{2+} concentrations are shown. Bars represent the standard deviation (n = 3 experiments). A submicromolar concentration of Ca^{2+} did not affect chromatin structure *in vitro*.

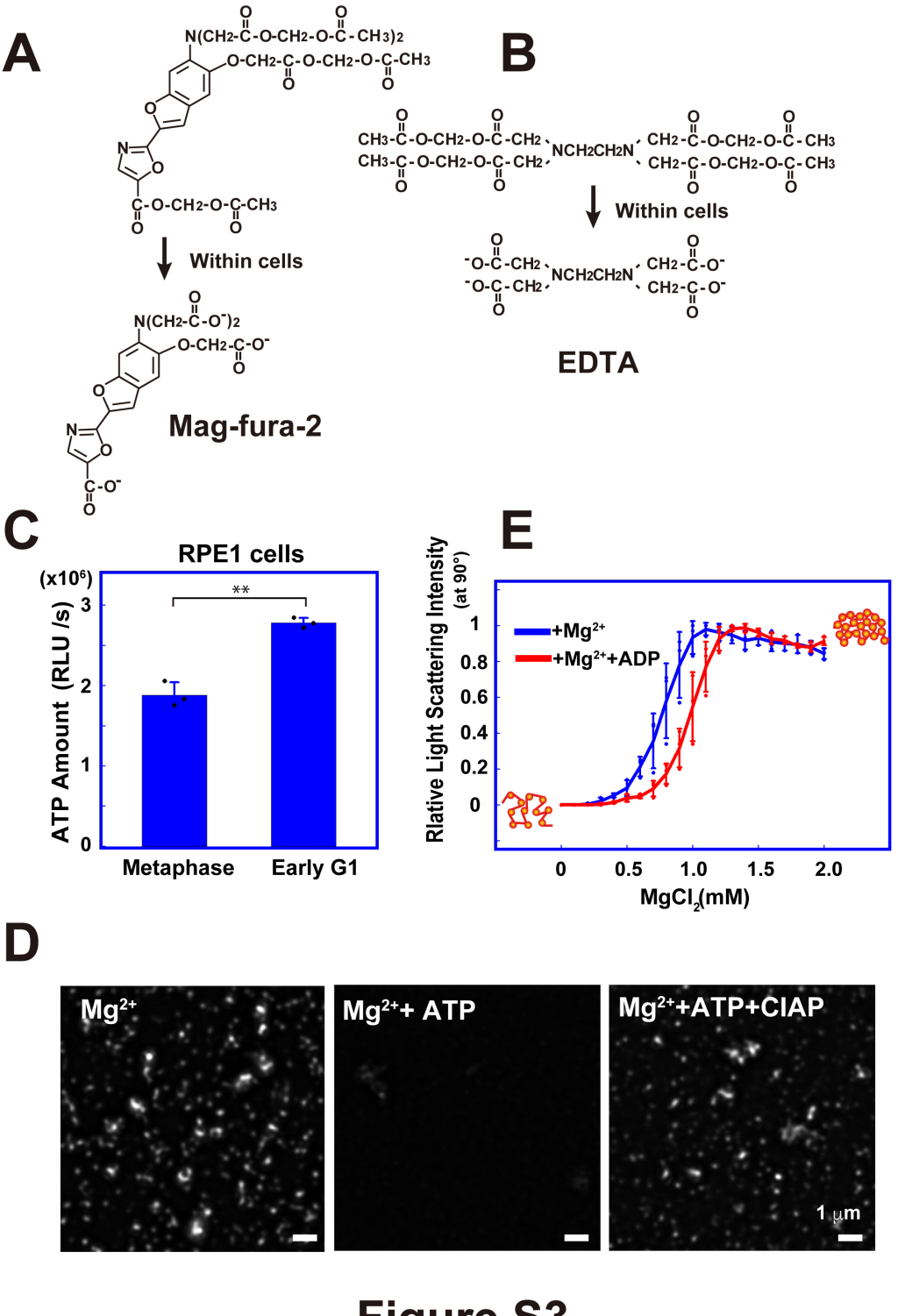
A
B
Within cells
Mag-fura-2
Within cells
EDTA
C
RPE1 cells
(x10⁶)
ATP Amount (RLU /s)
**
Metaphase
Early G1
E
Rlative Light Scattering Intensity (at 90°)
+Mg²⁺
+Mg²⁺+ADP
MgCl₂(mM)
D
Mg²⁺
Mg²⁺+ ATP
Mg²⁺+ATP+CIAP
1 μm

Figure S3

Figure S3, related to Figures 2 and 3.

(A and **B)** Structures of the cell-permeable Mag-Fura-2-AM (acetoxymethyl ester) (A) and ethylenediaminetetraacetic acid, acetoxymethyl ester (EDTA-AM) (B). These compounds were loaded into cells to generate intracellular Mag-Fura-2 (A) and EDTA (B) to capture Mg^{2+}. **(C)** Luciferase-based ATP measurements for synchronized human RPE1 cells (0.5×10^5 cells): metaphase cells (left) and early G1 cells (right). Bars represent the standard deviation. n = 3 experiments. **p < 0.001, Student's *t*-test ($p = 7.8 \times 10^{-4}$). **(D)** Fluorescent microscopic images of chromatin (related to Figure 3F). **(E)** The effects of ADP (apparent K_d = ~1 mM) on Mg^{2+}-dependent chromatin condensation. Bars represent the standard deviation (n = 3 experiments). Compared to ATP, the plots were slightly shifted and the effects of ADP were approximately half as strong.

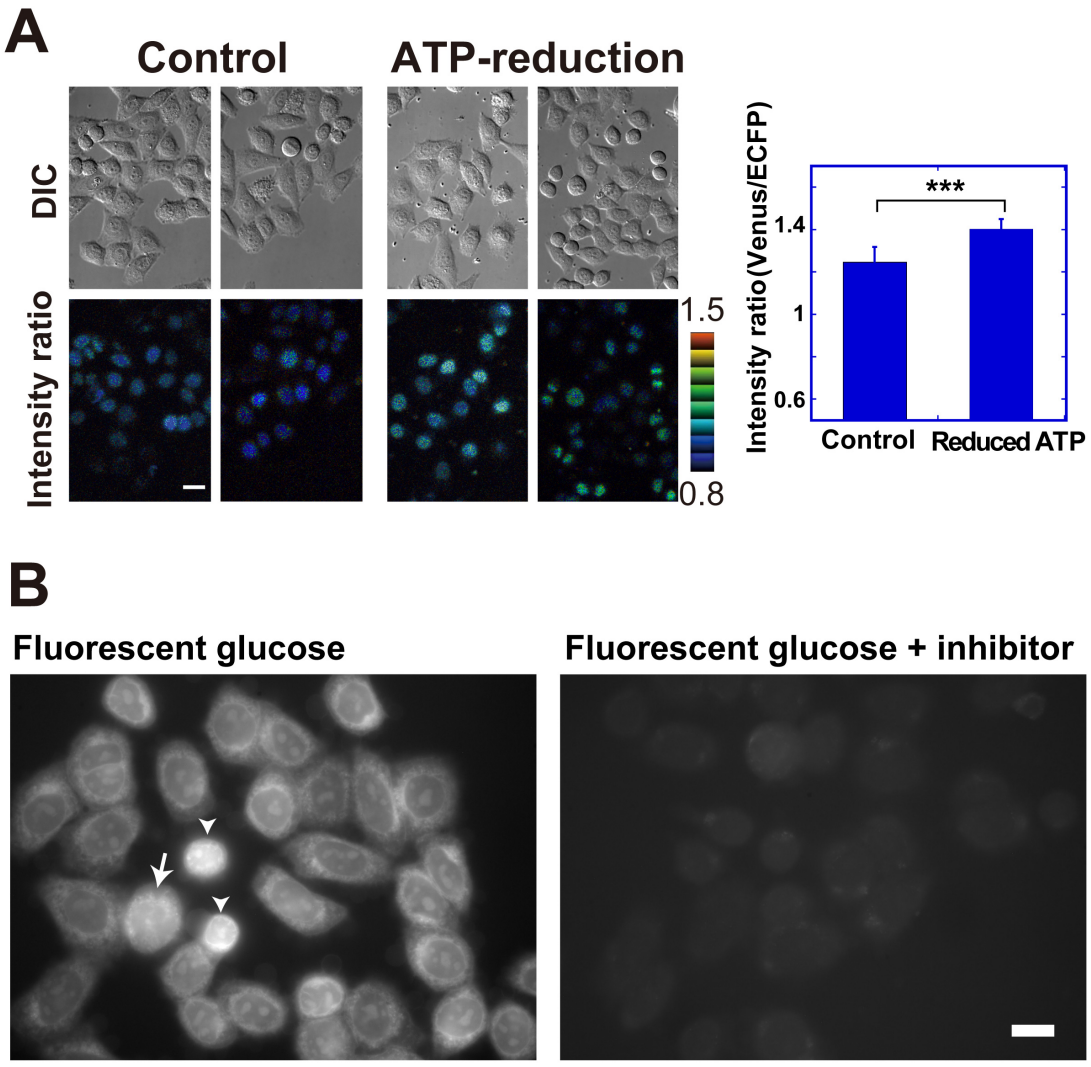
A
Control
ATP-reduction
DIC
Intensity ratio
1.5
0.8
Intensity ratio(Venus/ECFP)
***
1.4
1
0.6
Control
Reduced ATP
B
Fluorescent glucose
Fluorescent glucose + inhibitor

Figure S4

Figure S4, related to Figure 4.

(A) Comparison of Mg^{2+} levels between HeLa S3 cells expressing NLS-MARIO under normal (left) and ATP-reduction (center) conditions. Differential interference contrast microscopy (upper, DIC) images and pseudocolored emission ratio images (lower, intensity ratio) of MARIO expressed in asynchronous HeLa S3 cells. Average ratios are presented on the bar graph (right). n = 55 cells for each condition. Scale bar, 20 μm. ***$p < 0.0001$, Welch's *t*-test ($p = 2.2 \times 10^{-16}$). Note that the detected increase in Mg^{2+} may be underestimated, because chromatin can absorb Mg^{2+} and reduce the FRET ratios (Figure S1H). (**B**) Uptake of the fluorescent glucose analog (2-NBDG) [S5] in interphase and mitotic (arrow) cells (left). Upon treatment with the glucose transporter inhibitor pholoretin, the cells exhibited almost no fluorescent signal (right). Scale bars, 10 μm. Note that uptake in mitotic cells is as high as or even higher than that in interphase cells.

Table S1, related to Figure 3.

KEGG ID	Compound Name	m/z	Amount (fmol/cell)	
			Mitotic HeLa S3	Early G1
C00020	AMP	346.0558	0.027	0.033
C00008	ADP	426.0221	0.16	0.23
C00063	CTP	481.9772	0.16	0.17
C00075	UTP	482.9613	0.50	0.58
C00002	ATP	505.9885	0.59	1.6
C00044	GTP	521.9834	0.034	0.27
C00073	Met	150.0583	1.6	1.2
C00407	Ile	132.1019	6.7	5.0
C00123	Leu	132.1019	7.3	5.4
C00047	Lys	147.1128	1.2	1.0
C00135	His	156.0768	1.6	1.2
C00079	Phe	166.0863	3.4	2.6
C00214	Thymidine	243.0975	2.9	1.9
C00300	Creatine	132.0768	0.94	0.93
C00003	NAD+	662.1019	0.58	0.51

Results of metabolomic analysis based on capillary electrophoresis-based mass spectrometry (CE-MS) [S6] for detected nucleotides, amino acids, and other metabolites. The values are shown as the average of two independent analyses. Note that these molecules represent the total molecules extracted from cells.

Table S2, related to Figures 1-4.

KEGG ID	Compound Name	m/z	Amount (fmol/cell)		
			Mitotic HeLa S3	Early G1	
C00103	G1P	259.0224	0.030	0.034	Glycolysis
C00092	G6P	259.0224	0.44	0.53	Glycolysis, Pentose Phosphate Pathway
C00085	F6P	259.0224	0.14	0.18	Glycolysis, Pentose Phosphate Pathway
C00354	F1,6P	338.9888	0.042	0.026	Glycolysis, Pentose Phosphate Pathway
C00111	DHAP	168.9908	0.33	0.073	Glycolysis, Pentose Phosphate Pathway
C00093	Glycerophosphate	171.0064	0.97	0.23	Glycolysis, Pentose Phosphate Pathway
C00661	G3P	168.9908	0.033	N.D.	Glycolysis, Pentose Phosphate Pathway
C01159	2,3-DPG	264.9520	N.D.	N.D.	Glycolysis
C00197	3PG	184.9857	0.022	0.017	Glycolysis
C00631	2PG	184.9857	0.029	0.023	Glycolysis
C00074	PEP	166.9751	N.D.	N.D.	Glycolysis, TCA Cycle
C00022	Pyruvate	87.0088	N.D.	N.D.	Glycolysis, TCA Cycle, Pentose Phosphate Pathway
C00186	Lactate	89.0244	5.4	3.2	Glycolysis, TCA Cycle
C00352	Glucosamine 6-phosphate	258.0384	N.D.	N.D.	Glycolysis, TCA Cycle
C00024	Acetyl CoA	403.5556	N.D.	N.D.	Glycolysis, TCA Cycle
C00158	Citrate	191.0197	0.26	0.46	TCA Cycle
C00417	cis-Aconitate	173.0092	0.0094	0.016	TCA Cycle
C00311	Isocitrate	191.0197	N.D.	N.D.	TCA Cycle
C00026	2-Oxoglutarate	145.0142	0.093	0.096	TCA Cycle
C02630	2-Hydroxyglutarate	147.0299	0.022	0.019	Onco Metabolite
C00091	Succinyl CoA	432.5584	N.D.	N.D.	TCA Cycle
C00042	Succinate	117.0193	0.13	0.18	TCA Cycle
C00122	Fumarate	115.0037	0.098	0.18	TCA Cycle
C00711	Malate	133.0142	0.48	0.74	TCA Cycle
C00345	6-Phosphogluconate	275.0174	0.020	0.028	Pentose Phosphate Pathway
C00199	Ru5P	229.0119	0.055	0.019	Pentose Phosphate Pathway
C00117	R5P	229.0119	0.019	0.0080	Pentose Phosphate Pathway
C05382	S7P	289.0330	0.066	0.14	Pentose Phosphate Pathway
C00003	NAD+	662.1019	0.58	0.51	
C00004	NADH	664.1175	0.026	0.024	

Results of metabolomic analysis based on CE-MS [S6] for detected metabolites in glycolysis, the TCA cycle, and pentose phosphate pathways. N.D., not detected. The

values are shown as the average of two independent analyses. Note that these molecules represent the total molecules extracted from cells.

Supplemental References

S1. Grynkiewicz, G., Poenie, M., and Tsien, R.Y. (1985). A new generation of Ca2+ indicators with greatly improved fluorescence properties. J Biol Chem *260*, 3440-3450.

S2. Lipfert, J., Doniach, S., Das, R., and Herschlag, D. (2014). Understanding nucleic acid-ion interactions. Annu Rev Biochem *83*, 813-841.

S3. Maeshima, K., Rogge, R., Tamura, S., Joti, Y., Hikima, T., Szerlong, H., Krause, C., Herman, J., Seidel, E., DeLuca, J., et al. (2016). Nucleosomal arrays self-assemble into supramolecular globular structures lacking 30-nm fibers. EMBO J *35*, 1115-1132.

S4. Dimitrov, S.I., Apostolova, T.M., Makarov, V.L., and Pashev, I.G. (1986). Chromatin superstructure. A study with an immobilized trypsin. FEBS Lett *200*, 322-326.

S5. Yoshioka, K., Takahashi, H., Homma, T., Saito, M., Oh, K.B., Nemoto, Y., and Matsuoka, H. (1996). A novel fluorescent derivative of glucose applicable to the assessment of glucose uptake activity of Escherichia coli. Biochimica et biophysica acta *1289*, 5-9.

S6. Soga, T., Igarashi, K., Ito, C., Mizobuchi, K., Zimmermann, H.P., and Tomita, M. (2009). Metabolomic profiling of anionic metabolites by capillary electrophoresis mass spectrometry. Anal Chem *81*, 6165-6174.